Karlsruhe Institute of Technology

# Design and Measurement of Superconducting Spiral Microwave Resonators

# Entwurf und Vermessung supraleitender Spiralmikrowellenresonatoren

Bachelor Thesis of


Egor Kiselev

Department of Physics
Physikalisches Institut (PI)


Reviewer: Prof. Dr. Alexey Ustinov
Advisor: Dr. Martin Weides

Duration:: February 2013 – August 2013

I declare that I have developed and written the enclosed thesis completely by myself, and have not used sources or means without declaration in the text.

**Karlsruhe, 28. August 2013**

. . . . . . . . . . . . . . . . . . . . . . . . . . . . . . . . . . . . . . .

(**Egor Kiselev**)

# Design and Measurement of Superconducting Microwave Spiral Resonators

Egor Kiselev

September 4, 2013, Karlsruhe

# Contents

# Introduction

The developement of so called metamaterials is currently a large area of research. Metamaterials are artificially made materials, which exhibit unusual electromagnetic properties, the most famous example being a material with a negative refraction index $n < 0$. Negative refraction index metamaterials are known to have most useful applications, such as building a flat lense without an optical axis, thus perfectly linear in its behavior [1].

A material's response to applied electromagnetic fields is characterised by its magnetic permeability $\mu$ and electric permittivity $\epsilon$. $n < 0$ requires $\mu < 0$ and $\epsilon < 0$ simultaneously [2]. $\mu < 0$ can be obtained by periodically arranging planar electromagnetic resonators on a surface, whereas a negative permittivity is approached through an array of thin conductive wires [1]. A necessary condition for an arrangement of elements to effectively behave as a medium allowing electromagnetic wave propagation is that the scale representing the arrangement's periodicity $s$ is much smaller than the length $\lambda$ of waves transmitted through it: $s \ll \lambda$. In other words: the medium has to be sufficiently homogeneous, hence compact elements are favorable.

The idea to use superconducting spiral resonators to build a negative refraction metamaterial was recently proposed [3],[4]. Because of their small sizes and low losses they are promising metamaterial building blocks. This work deals with the practical task of designing single spiral superconducting microwave resonators and the study of their properties through simulations and measurement. It also provides an overview of the basic properties of superconductors and of lumped element resonator theory.

# Chapter 1

# Basics of Superconductivity

Since in our case a superconductor is used for the fabrication of microwave resonators, some important properies of such a material as well as some basic theoretical concepts of superconductivity shall be discussed in this chapter.

## 1.1 Critical Temperature, Resistance and Diamagnetism of Superconductors

The most striking property of a superconductor is, that below a critical temperature $T_C$ its specific resistance $\rho$ vanishes, which was discovered as early as 1911 by H. Kamerlingh Onnes. The superconductor studied was mercury with a critical temperature of 4.2 K (see Fig. 1.1). Today many materials are known to exhibit superconducting properties below a critical temperature, which is material specific. On the other hand good room temperature conductors such as copper and silver do not behave as superconductors even at lowest temperatures. Here as the temperature approaches zero the specific resistance approaches a constant value, the so called residual resistance, which is due to lattice impurities (see Fig. 1.2).

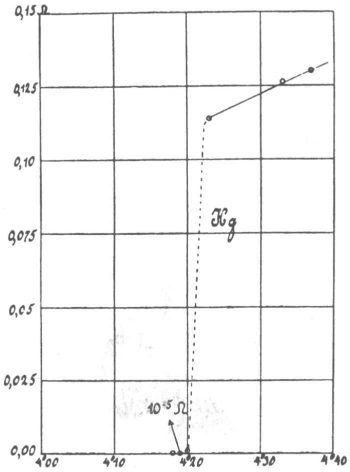


Figure 1.1: Kammerlingh Onnes' diagram of the resistance of his mercury sample marking the discovery of superconductivity in 1911. Below a critical temperature the resistance vanishes. (After [5])

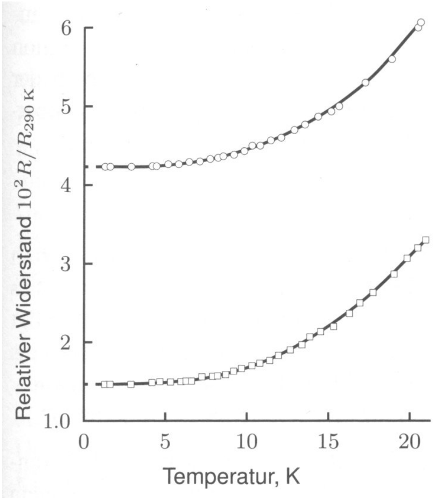


Figure 1.2: Not all materials are superconductors. Relative resistances ($R/R_{290\mathrm{K}}$) of two Kalium samples against temperature are shown. Residual resistance is due to lattice defects, hence the different values at low temperatures show that the samples had different defect concentrations. (Copied from [6], p. 169)

Though in a superconductor we have a material with $\rho = 0$, we must carefully distinguish it from an ideal conductor. In an ideal conductor by definition the electric potential $\Phi$ is constant and hence the electric field $\mathbf{E}$ vanishes. Then by Maxwell's equations

$$-\partial_t \mathbf{B} = \nabla \times \mathbf{E} = 0 \ , \tag{1.1}$$

meaning that inside an ideal conductor magnetic fields are constant in time. The behavior of superconductors is different. It was observed that a superconducting bulk acts as an ideal diamagnet, in other words: being placed in an outer magnetic field $\mathbf{H}_{\mathrm{out}}$ it expels this field from its inside so that its magnetisation is $\mathbf{M} = -\mathbf{H}_{\mathrm{out}}$ [6].

To explain this effect named after Meissner and Ochsenfeld a closer look must be taken at the currents inside a superconductor. For the density $\mathbf{j}$ of an homogeneous current we have

$$\mathbf{j} = \frac{nq}{m}\mathbf{p} \ , \tag{1.2}$$

where $n$ is the charge carrier density, $q$ the charge of a carrier, $m$ its mass and $\mathbf{p}$ the momentum of any charge carrier in the current. To treat the problem by means of quantum mechanics we assume that the wave function of charge carriers is given by $\psi(\mathbf{r}) = \psi_0 e^{i\theta(\mathbf{r})}$. The assumtion implies a constant charge carrier density $|\psi(\mathbf{r})|^2 = |\psi_0|^2$ everywhere inside the superconductor. To calculate the momentum we apply the momentum operator to $\psi(\mathbf{r})$. In presence of an outer magnetic field we obtain the proper momentum operator by replacing the kinetic by the canonical momentum [7]: a method known as minimal coupling.

$$\mathbf{p} = \frac{\hbar}{i}\nabla \ \rightarrow \ \mathbf{p}_{\text{field}} = \frac{\hbar}{i}\nabla - q\mathbf{A} \ . \tag{1.3}$$

Here $\mathbf{A}$ is the vector potential so that $\nabla \times \mathbf{A} = \mathbf{B}$. Applying $\mathbf{p}_{\text{field}}$ to the wave function yields in

$$\mathbf{p}_{\text{field}} \ \psi(\mathbf{r}) = \big(\hbar\nabla\theta(\mathbf{r}) - q\mathbf{A}\big)\psi(\mathbf{r}) \ . \tag{1.4}$$

Using (1.2) we finally obtain

$$\mathbf{j} = \frac{nq}{m}\big(\hbar\nabla\theta(\mathbf{r}) - q\mathbf{A}\big) \tag{1.5}$$

and taking the curl of both sides:

$$\nabla \times \mathbf{j} = -\frac{nq^2}{m}\mathbf{B} \ , \tag{1.6}$$

because the curl of a gradient field vanishes. Equation 1.6 is called the first London equation. It offers the following explanation to the Meissner-Ochsenfeld effect: Since by a Maxwell equation $\nabla \times \mathbf{B} = \mu_0 \mathbf{j} + \mu_0 \epsilon_0 \partial_t \mathbf{E}$ and in our case there will be no time dependent electric fields, it is $\nabla \times \big(\nabla \times \mathbf{B}\big) = -\nabla^2 \mathbf{B} = -\frac{\mu_0 n q^2}{m}\mathbf{B}$. This equation is called second London equation and $\big(\frac{\mu_0 n q^2}{m}\big)^{-1/2} = \lambda$ is called the London penetration depth. The equation indicates that superconductors expel magnetic fields, which can be shown by solving it for the simple case of a planar superconducting bulk of thickness $d$, placed parallel to the field lines of an homogeneous magnetic field. Disregarding edge effects the above equation can be simplified to $\partial_x^2 B = \lambda^{-1} B$, where the $x$ axis lies perpendicular to the bulk surface at $x = 0$. Then $B = B_{x=0} e^{-x/\lambda}$ meaning that if $\lambda \ll d$ inside the bulk $B = 0$ holds. Since $\mathbf{B} = \mu_0(\mathbf{H}_{\text{out}} + \mathbf{M})$ we have $\mathbf{H}_{\text{out}} = -\mathbf{M}$ as quoted above or in terms of susceptibility $\chi = -1$.

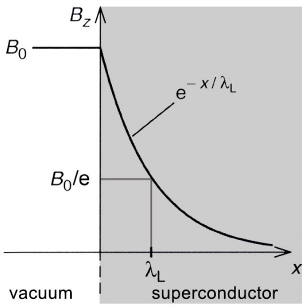


Figure 1.3: Illustration of the behavior of an homogeneous magnetic field inside a superconductor. The field is parallel to the superconductor surface, the field strength decreases exponentially as described by the second London equation. (Copied from [8])

Common values for $\lambda$ are of the order of tens of nm, so that a bulk superconductor will behave as an ideal diamagnet. Figure 1.4 illustrates the difference in behavior of ideal and superconductors.

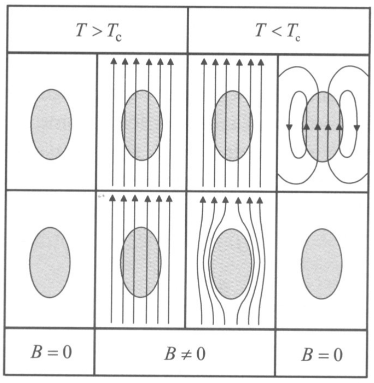


Figure 1.4: Behavior of a hypothetical material becoming an ideal conductor below a critical temperature $T_C$ (top) and a superconductor with the same $T_C$ (bottom). Inside an ideal conductor magnetic fields do not change with time, whereas the superconductor shows the Meissner Ochsenfeld effect and expels the field. (Copied from [9], p. 457)

One consequence of the Meissner-Ochsenfeld effect is that superconducting currents flow on the surface of a superconductor, otherwise magnetic fields inside the superconductor would appear. In fact it can be shown by further application of Maxwell's equations that an electric field $\mathbf{E}$ inside the superconductor also has to obay the equation $\nabla^2\mathbf{E} = -\frac{\mu_0 nq^2}{m}\mathbf{E}$ [10].

It is essential to our discussion, that we considered superconducting charge carriers to be of bosonic nature. Otherwise in the above derivation further complications due to Fermi-Dirac statistics would arise. For example in case of fermionic charge carriers it is known that only those carriers located on the Fermi surface can support an electric current. As we will see superconducting charge carriers in fact are bosonic.

## 1.2 Flux Quantization, Classification of Superconductors in Types I and II, BCS Theory

### 1.2.1 Flux Quantization

The magnetic flux through a superconducting ring (see Fig. 1.5) is quantized in whole number multiples of the flux quantum $\Phi_0 = \frac{h}{q}$, where $h$ denotes Planck's constant and $q$ is the charge of a single superconducting charge carrier. In other words: flux is quantized. This can be explained using equation (1.5). As discussed in section 1.1 inside the superconductor no currents flow. From (1.5) we get $\nabla\theta = \frac{q}{\hbar}\mathbf{A}$ and integrating over the closed loop C (Fig. 1.5) yields:

$$\oint_c \nabla\theta d\mathbf{s} = \frac{q}{\hbar}\oint_c \mathbf{A}\cdot d\mathbf{s}\ . \tag{1.7}$$

Stokes' theorem together with $\nabla\times\mathbf{A} = \mathbf{B}$ gives

$$\oint_c \nabla\theta d\mathbf{s} = \frac{q}{\hbar}\int \mathbf{B}\cdot d\mathbf{s}\ , \tag{1.8}$$

where the second integral is over the inner surface of the ring and gives the total flux through the ring. The first integral, if not carried out over the whole loop, but between the two points 1 and 2 gives: $\int_1^2 \nabla\theta d\mathbf{s} = \theta_2 - \theta_1$. For a well behaved $\theta(\mathbf{r})$ the closed integral should vanish. However it is not of physical importance that $\theta(\mathbf{r})$ is well behaved, but that $e^{i\theta(\mathbf{r})}$ is well defined at every point $\mathbf{r}$

$$\oint_c \nabla\theta d\mathbf{s} = 2\pi n \tag{1.9}$$

holds, where n is an integer number[1]. Obviously under such a condition $e^{i\theta(\mathbf{r})}$ is well defined at the point $\mathbf{r}_0$. On the other hand $\oint_c \nabla\theta d\mathbf{s} = 2\pi n \neq 0$ becomes possible. Putting eq. (1.9) and eq. (1.8) together we see, that if the total flux inside the ring $\Phi = \int \mathbf{B}\cdot d\mathbf{s}$ does not vanish, it is necessarily

$$\Phi = \frac{2\pi\hbar n}{q} = \frac{h}{q}\ n \tag{1.10}$$

and flux is quantized. Figure 1.6 shows a measurement of quantized flux.

[1] If we are not too concerned with uniqueness of $\theta$ at every point, a function satisfying (1.9) is not hard to find. For example $\theta = \phi$, where $\phi$ is the polar angle, satisfies (1.9).

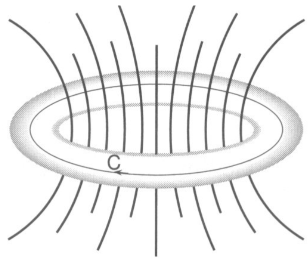


Figure 1.5: Magnetic flux inside a superconducting ring. The area through which the flux flows is not superconducting. Integration path C is shown. ([6], p. 308)

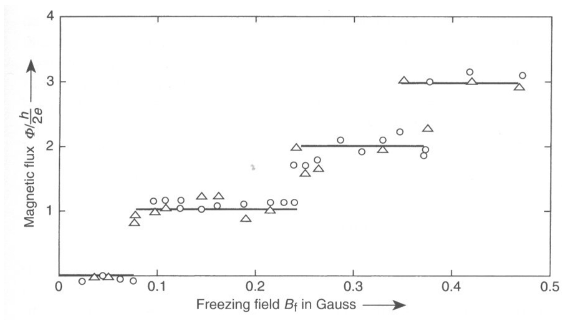


Figure 1.6: Measurement of magnetic flux quantization in a Sn cylinder. Flux comes in quanta of $\Phi_0 = \frac{h}{2e}$. ([11], p. 30)

### 1.2.2 Type I and Type II Superconductors

Type I and type II superconductors show different magnetisation properties. A type I superconductor expels an applied magnetic field completely until it reaches a critical value $H_C$. Above $H_C$ the material shows no superconductivity. A type II superconductor expels an applied magnetic field completely until it reaches a critical value $H_{C1}$. Above $H_{C1}$ the magnetic field is expelled only partly. This state is called the vortex state. Finally above a second critical value $H_{C2}$ the superconductivity vanishes. Figure 1.7 visualizes this behavior.

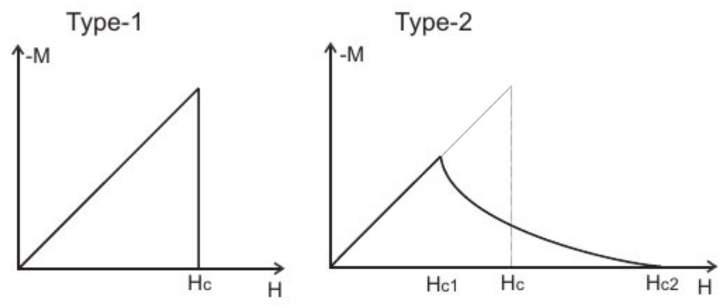


Figure 1.7: Magnetization depending on applied outer magnetic field H. In Type 1 materials superconductivity breaks down at a critical field $H_c$. In Type 2 superconductors above $H_{c1}$ magnetic fields are expelled only partly. Here superconductivity breaks down at a higher outer field $H_{c2}$ (after [12])

.

Typically $H_C$ and $H_{C1}$ are quite low and $H_{C1} \ll H_{C2}$. To distinguish between both superconductor types more precisely the coherence length $\xi$ must be introduced. It is the length beneath which electromagnetic fields varying in space have no considerable influence on superconducting charge carrier density. Hence to calculate $\mathbf{j}$ fields must be averaged over $\xi$. Later $\xi$ will be defined more carefully. As stated in [6] following distinction can be made: London penetration depth $\lambda < \xi$ for a type I superconductor, whereas $\lambda > \xi$ for a type II superconductor.

An important property of Type II superconductors is that between $H_{C1}$ and $H_{C2}$ magnetic fields can penetrate the superconductor in the form of so called Abrikosov vortices (hence $\mathbf{M} \neq -\mathbf{H}_{\text{out}}$ and the name vortex state). This is visualized in Figure 1.8. Inside a vortex the material is not in the superconducting but in the normal conducting state, hence flux quantization occurs and the flux inside a vortex is equal to $\Phi_0$. In presence of an electric field vortices can move inside the superconductor dissipating energy, however they tend to pin on crystal defects. To lower the energy dissipation due to Abrikosov vortices on a superconducting film so called pinning centers or flux traps, consisting of non-superconducting areas acting as artificial defects, can be placed (see section 3.1).

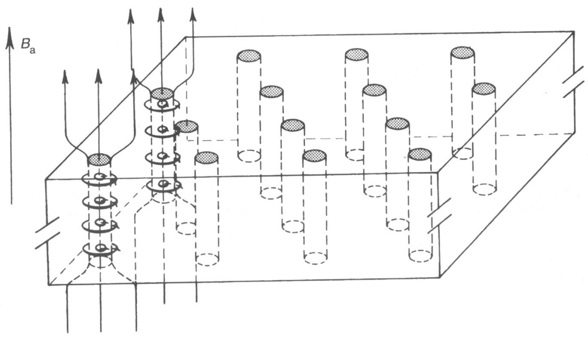


Figure 1.8: In a Type II superconductor an applied outer magnetic field penetrates the superconductor in the form of so called Abrikosov vortices. Inside the vortices material is not superconducting, hence flux quantization occurs. Every vortex carries on quantum of magnetic flux. Supercurrents supporting the flux are shown. ([13], p. 24)

### 1.2.3 BCS-Theory

The accepted microscopic theory on conventional superconductivity is the BCS (Bardeen, Cooper, Schrieffer) theory. It states that even a weak attractive force between electrons leads to an electronic energy ground state of electrons (BCS groundstate) that is separated from excited states by an energy gap of size $\Delta$ and lies below the Fermi level of ordinary electrons.

Attractive forces between electrons stem from scattered electrons deforming the lattice and making it possible for another electron to use this deformation to minimize its potential energy. The two electrons are then attracted to each other. This attraction can be described mathematically by the exchange of a (virtual) phonon between the two electrons (see Fig. 1.9). One might wonder, why the Coulomb force does not destroy such a subtle interaction. Here it is of importance that the processes of lattice deformation and Coulomb force act on significantly different timescales. The time the lattice takes to return to its original state is so long, that the scattered electron already is “too far away” for the Coulomb interaction between it and the arriving second electron to be of importance.

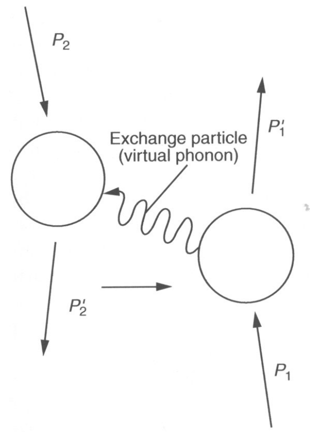


Figure 1.9: A Cooper pair. Two electrons with opposite momentum vectors are attracted by means of a virtual phonon exchange. Cooper pairs are the charge carriers of supercurrent. ([13], p. 117)

The attracted electrons as shown in Fig. 1.9 are called Cooper pairs. Electrons of a Cooper pair have wave vectors $\mathbf{k}$, $-\mathbf{k}$ and, which is most important, spins ($\uparrow$) showing in oposite directions (see [13], p. 115). Therefore Cooper pairs $\{\mathbf{k}\uparrow, -\mathbf{k}\downarrow\}$ are bosonic and can condense in the BCS groundstate. Measurements of quantized flux ($\Phi_0 = \frac{h}{q}$) show ([6], p. 308) that the charge $q$ of superconducting charge carriers is in fact $-2e$, meaning that supercurrents are supported by Cooper pairs.

Many electromagnetic properties of superconductors are consequences of the existance of the energy gap $\Delta$. Cooper pairs can not be decelerated by scattering on lattice defects, because there exist no energy states supporting such a process. The occurance of critical temperature $T_C$ also is explained by $\Delta$. Furthermore the BCS theory delivers a formula for coherence length $\xi_0 = 2\hbar v_F/\pi\Delta$ ([6], p.306), where $v_F$ is the Fermi velocity. In case of so called dirty superconductors with mean free path $l$ for electrons in the normal state it is $\xi = (\xi_0 \cdot l)^{1/2}$, which together with 1.2.2 explains why alloys and non-epitaxial thin films tend to be type II superconductors. For example pure lead is a type I superconductor, whereas an alloy of lead and 2% Indium becomes type II. NbN films, used for resonator fabrication in our case, also are type II superconductors.

## 1.3 Kinetic inductance

The energy stored in a magnetic field $\mathbf{H}, \mathbf{B}$ is given by $W = \frac{1}{2}\int_V \mathbf{H}\cdot\mathbf{B}\ d^3x$. For a wire through which current $I$ flows $W$ can also be expressed in terms of current [14]:

$$W = \frac{1}{2} L_{\text{geo}} I^2 \ , \tag{1.11}$$

where $L_{\text{geo}}$ is called inductance and depends on the geometry (curvature, length...) of the wire. Creating a magnetic field is not the only way a flowing current can store energy. The kinetic energy of charge carriers also can be of importance, however it is negligible for a normal conductor since, due to frequent scattering, electrons have no time to accumulate a great amount of kinetic energy beside their thermal energy which is not considered, because it is not caused by an electric field. Cooper pairs however are not scattered and therefore can store kinetic energy.

Consider a thin superconducting film of cross section $A$ and length $l$ with a homogeneous current density $j$. The total current is $I = jA$. The kinetic energy stored by the current is $E_{\text{kin}} = \sum \frac{p^2}{2m}$ where the sum is over all Cooper pairs. Assuming an homogeneous Cooper pair density $n_s$ we can write $E_{\text{kin}} = \frac{p^2}{2m} \cdot n_s \cdot A \cdot l$. From (1.2) we get $p = \frac{m}{n_s q} j$ and therefore using

$I = jA$:

$$E_{\text{kin}} = \frac{m}{2n_s q^2} \frac{l}{A} I^2 \ . \tag{1.12}$$

Since $E_{\text{kin}} \propto I^2$ in analogy to (1.11) we can write

$$E_{\text{kin}} = \frac{1}{2} L_{\text{kin}} I^2 \tag{1.13}$$

hereby defining the kinetic inductance $L_{\text{kin}}$. The total energy stored is $E_{\text{tot}} = E_{\text{kin}} + W = \frac{1}{2}\big(L_{\text{kin}} + L_{\text{geo}}\big)I^2$. Therefore total inductance is the sum of geometric and kinetic inductance. From this follows, that geometric and kinetic inductance behave equal in terms of ac impedances. The resonant frequency $1/\sqrt{LC}$ of an ordinary capacitance inductance resonator is lowered by a non vanishing kinetic inductance because of $L = L_{\text{geo}} + L_{\text{kin}}$.

# Chapter 2

# Resonator Theory

This chapter gives an overview of lumped element resonator theory. Scattering parameters are defined and discussed, as well as parallel, series RLC resonators and their quality factors. A lumped elements model of a spiral resonator capacitively coupled to a feedline is proposed. Methodes for determining quality factors from simulations are derived from the model.

## 2.1 The Transmission Line

A transmission line (TL) consists of two conductors linked through capacitance C and inductance L, whose values depend upon material properties and geometrical distribution in space. In addition conductors will usually behave as ohmic resistors with resistance R. It is possible to discuss the properties of TLs using a lumped-element circuit model as shown in Fig. 2.1. Here R, L, C are defined as quantities per unit length and in order to take dielectric loss into account conductance G is introduced. $\Delta z$ marks a small length intervall along the TL.

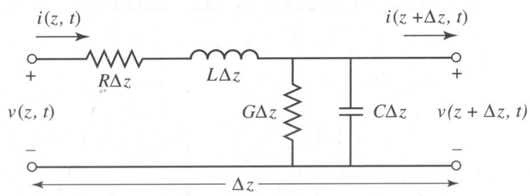


Figure 2.1: Lumped elements model of a transmission line section of length $\Delta z$. The section contributes an Ohmic resistance $R\Delta z$ an inductance $L\Delta z$ a capacitance $C\Delta z$. Conductance $G\Delta z$ takes dielectric losses into account. ([15], p. 50)

Analysing this circuit we follow Ref. [15]. In this section we will denote the imaginary number as $j$ to reserve $i$ for the time dependent total current through a conductor. By Kirchhoff's voltage law from Fig. 2.1 we have:

$$v(z,t) - R\Delta z i(z,t) - L\Delta z \frac{\partial i(z,t)}{\partial t} - v(z+\Delta z,t) = 0, \tag{2.1}$$

and by the Kirchhoff's current law, it is:

$$i(z,t) - G\Delta z v(z+\Delta z,t) - C\Delta z \frac{\partial v(z+\Delta z,t)}{\partial t} - i(z+\Delta z,t) = 0. \tag{2.2}$$

Dividing (2.1) and (2.2) by $\Delta z$ results in (2.3) and (2.4), if $\Delta z \to 0$.

$$\frac{\partial v(z,t)}{\partial z} = -Ri(z,t) - L\frac{i(z,t)}{\partial t} \tag{2.3}$$

$$\frac{\partial i(z,t)}{\partial z} = -Gv(z,t) - L\frac{v(z,t)}{\partial t} \,. \tag{2.4}$$

Assuming oscillating voltages and currents $v(z,t) = V(z)e^{j\omega t}$ and $i(z,t) = I(z)e^{j\omega t}$ (2.3) and (2.4) can be rewritten as

$$\frac{dV}{dz} = -(R + j\omega L)I \tag{2.5}$$

$$\frac{dI}{dz} = -(G + j\omega C)V \,. \tag{2.6}$$

General solutions to this first order coupled ordinary differential equations are

$$V(z) = V_0^+ e^{-\gamma z} + V_0^- e^{\gamma z} \tag{2.7}$$

$$I(z) = I_0^+ e^{-\gamma z} + I_0^- e^{\gamma z} \,, \tag{2.8}$$

implying that wave propagation is possible in +z direction (hence $V_0^+$, $I_0^+$) and -z direction. $\gamma = \sqrt{(R + jwL)(G + jwC)} = \alpha + j\beta$ is called propagation constant. By plugging (2.7) into (2.5) we see that

$$I(z) = Z_0\big(V_0^+ e^{-\gamma z} - V_0^- e^{\gamma z}\big) \,, \tag{2.9}$$

where $Z_0 = \frac{\gamma}{R+j\omega L}$ is called characteristic impedance.

### 2.1.1 Reflection and Transmission Coefficients

In this section we assume a low loss or lossless transmission line, so that the amplitudes of voltage and current are constant along the TL. Consider a terminated TL as shown in Fig. 2.2. By definition it is $Z_L = \frac{V(z=0)}{I(z=0)}$. From (2.7), (2.9) we see $Z_L = \frac{V_0^+ + V_0^-}{V_0^+ - V_0^-} Z_0$, so that

$$\frac{V_0^-}{V_0^+} = \frac{Z_L - Z_0}{Z_L + Z_0} =: \Gamma \,. \tag{2.10}$$

The ratio between amplitudes of incident and reflected waves $\Gamma$ is called reflection coefficient. Note that $\Gamma = 0$ if $Z_L = Z_0$, so no waves are reflected.

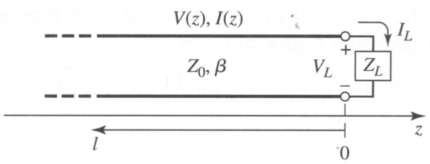


Figure 2.2: Transmission line with characteristic impedance $Z_0$ and propagation constant $j\beta$ terminated at $z = 0$ in an impedance $Z_L$. ([15], p.58)

To calculate the transmission coefficient T we imagine that the TL is not terminated at z = 0 but connected to another TL with a different characteristic impedance $Z_1$ (Fig. 2.3).

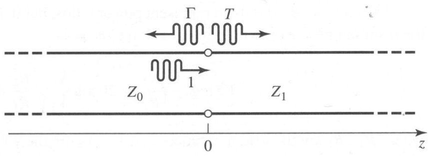


Figure 2.3: Illustration of transmission and reflection of waves at a connection of TLs of different characteristic impedances. ([15], p.63)

(2.7) can be rewritten as $V(z) = V_0^+\left(e^{-j\gamma z} + \Gamma e^{j\gamma z}\right)$. Assuming the second TL is terminated in $Z_1$ somewhere at $z > 0$, there is no reflection except at z = 0. Thus for $z > 0$ we write $V_1(z) = V_0^+ T e^{-\gamma z}$, hereby defining the transmission coefficient T. At z = 0 it is $V(0) = V_1(0)$, so that

$$T = 1 + \Gamma = \frac{2Z_1}{Z_1 + Z_0}\,. \tag{2.11}$$

## 2.2 Scattering Parameters of a Two Port

During this work a spiral resonator coupled to a feedline is considered to be a two port network. Abstractly speaking a two port networt (short: two port) consists of a "black box"[1] and four terminals (see Fig. 2.4). Two terminals respectively form a port, which can be connected to a TL.

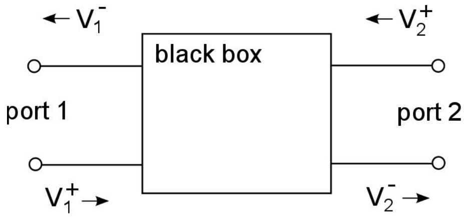


Figure 2.4: An abstract two port. $V_i^{+/-}$ are the amplitudes of incident or reflected voltage waves. The black box may contain some unknown circuitry.

The so called scattering parameters can be defined by

$$S_{ij} = \frac{V_i^-}{V_j^+}\,, \tag{2.12}$$

where $i,\ j$ indicate at which port voltage amplitude is measured and where - / + indicate the amplitude of waves leaving / entering the "black box". In our case the "black box" has an impedance $Z_{box}$ and the TL leading to port 2 is terminated in an impedance that equals its characteristic impedance $Z_0$, to avoid wave reflection at the port (see Fig. 2.5).

[1] in our case containing the resonator

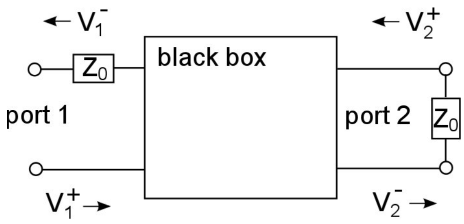


Figure 2.5: In simulations we will concider a two port where one of the ports is terminated to avoid wave reflections. The scattering parameters are calculated taking this termination into account.

Effectivly such a two port is a TL[2] with characteristic impedance $Z_0$ terminated in an impedance $Z_{\text{eff}}$. Depending on the box circuitry it is $Z_{\text{eff}} = Z_{\text{box}} + Z_0$ or $Z_{\text{eff}} = Z_{\text{box}}||Z_0$. The symbol $a||b$ stands for $a$ and $b$ being cirquited parallel. Now the expressions for the scattering parameters can be obtained in terms of impedances. By (2.10) and (2.11) we know that

$$S_{11} = \Gamma = \frac{Z_{\text{eff}} - Z_0}{Z_{\text{eff}} + Z_0} \tag{2.13}$$

and

$$S_{21} = T = \frac{2Z_{\text{eff}}}{Z_{\text{eff}} + Z_0}\,. \tag{2.14}$$

## 2.3 Resonant Circuits and Quality Factors

### 2.3.1 Series RLC Resonant Circuit

A series RLC is shown in Fig. 2.8. Its input impedance is $Z_{in} = R + j\omega L + \frac{1}{j\omega C}$ and the resonance frequency is $\omega_0 = \frac{1}{\sqrt{LC}}$, implying that $|Z_{in}|$ at resonance is minimal and $Z_{in}(\omega_0) = R$ is real.

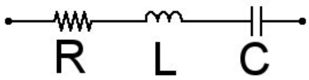


Figure 2.6: Series RLC contour consisting of resistor R, inductance L and capacitance C.

An important parameter of a resonant cirquit is its quality factor Q, indicating how well the cirquit stores energy. It is defined as

$$Q = \omega\frac{\text{average energy stored}}{\text{energy loss per time unit}} = \omega\frac{W_m + W_e}{P_l}\,, \tag{2.15}$$

where $W_m = \frac{1}{4}|I|^2 L$ is the average energy stored in magnetic fields, $W_e = \frac{1}{4}|V_C|^2 C = \frac{1}{4}|I|^2\frac{1}{\omega^2 C}$ the average energy stored in electric fields and $P_l = \frac{1}{2}|I|^2 R$ the average power dissipated. The additional factor $\frac{1}{2}$ in this equations origins in averaging over the sinusoidal time dependences of $I$ and $V$. Plugging this into (2.15) gives $Q_{\omega_0} = \frac{1}{\omega_0 RC}$.
For a small $\Delta\omega = w - w_0$ the impedance of a series RLC can be approximated by

$$Z_{in} \approx R + j\frac{2RQ\Delta\omega}{\omega_0} = R + j2L\Delta\omega\,. \tag{2.16}$$

Using this result it can be shown[3] that

$$Q \approx \frac{\omega_0}{BW_\omega}\,, \tag{2.17}$$

[2]namely the TL leading to port 1.
[3]See [15], p. 268f for further details.

where $BW_\omega$ is the width of $|Z_{in}|$-curve at $|Z_{in}| = \frac{1}{\sqrt{2}}R$ (see Fig. 2.7). This approximation is reasonable for large quality factors, where $\Delta\omega$ is small.

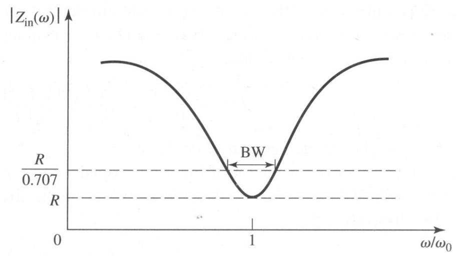


Figure 2.7: Input impedance of a series RLC. Illustration of determing $Q_\text{i}$ by measuring the width of $|Z_{in}|$-curve. ([15], p.267)

### 2.3.2 Parallel RLC Resonant Circuit

The input impedance of a parallel RLC circuit is given by $|Z_{in}| = \frac{1}{\frac{1}{R}+\frac{1}{j\omega L}+j\omega C}$, its resonant frequency is $\omega_0 = \frac{1}{\sqrt{LC}}$ and its quality factor is $Q = \omega_0 RC$. For a small $\Delta\omega = w - w_0$ the impedance can be approximated by

$$Z_{in} \approx \frac{R}{1 + 2j\Delta\omega RC} = \frac{R}{1 + 2jQ\Delta\omega/\omega_0}\,, \tag{2.18}$$

At resonance $|Z_{in}|$ is maximal, but the approximation

$$Q \approx \frac{\omega_0}{BW_\omega}\,, \tag{2.19}$$

still holds for a big Q[4]. The knowledge of parallel and series RLCs is useful, because many resonant circuits can be approximated by RLCs near resonance.

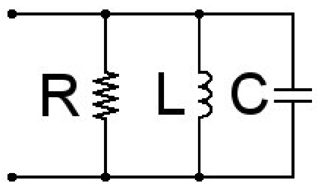


Figure 2.8: Parallel RLC contour consisting of resistor R, inductance L and capacitance C.

Until now only the internal energy loss of resonators was concidered, usually however the resonator is coupled to other circuitry, which lowers its overall $Q$. Let $Q_i$ be the resonator's internal quality factor. We define the coupling quality factor $Q_c$ such, that

$$\frac{1}{Q} = \frac{1}{Q_c} + \frac{1}{Q_i}\,. \tag{2.20}$$

[4]See [15], p. 270f for further details.

## 2.4 Lumped Element Model of a Spiral Resonator Coupled to a Feedline

Naively one can picture a spiral resonator (Fig. 2.10) as a wound up piece of open-cirquited TL (Fig. 2.9). An open circuited piece of TL behaves as a resonator by itself and its input impedance can be, at resonance, approximated[5] by $Z_{in} \approx \frac{Z_0}{\alpha l + j(\Delta\omega\pi/\omega_0)}$. Here $\alpha$ is the real part of propagation constant $\gamma$, l the TL's length and $Z_0$ its characteristic impedance. Comparing this expression for $Z_{in}$ to (2.18) we see, that at resonance an open circuited transmission line resonator behaves like a parallel RLC circuit. We therefore want to assume that the spiral, being a wound up open circuited TL, also will behave as a parallel RLC at resonance. Additionally the spiral is capacitively coupled to a feedline[6].

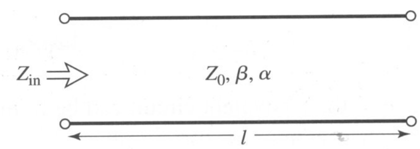


Figure 2.9: An open cirquited piece of transmission line with characteristic impedance $Z_0$ and propagation constant $\gamma = a + ib$ as shown here is by itself a resonator. It is resonable to concider a spiral resonator to be a wound up piece of an open circuited TL as done in our analysis. ([15], p.276)

Since in our simulations resonators are considered lossless, the resistance of the parallel RLC approaches infinity and can be neglected, thus leading to the lumped element model shown in Fig. 2.10.

[5]See [15] p. 276.

[6]Our approach is analogous to the one proposed in Ref. [16], where a waveguide resonator measured in transmission was concidered.

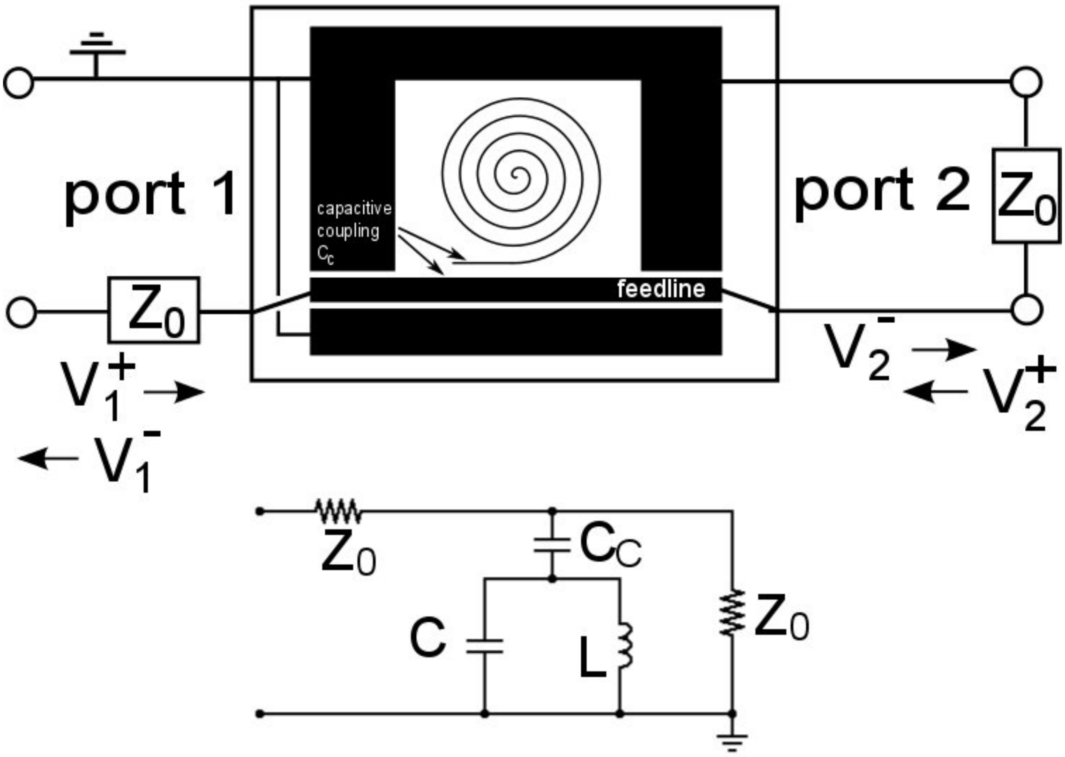


Figure 2.10: Illustration of the simulated two port cirquit (compare to Fig. 2.5) and the lumped elements model of the spiral resonator. $C_\mathrm{c}$ represents the resonator's capacitive coupling to the feedline and $C$, $L$ are properties of the resonator itself.

As seen from Fig. 2.10 $Z_\mathrm{box} = \frac{1}{\frac{1}{j\omega L}+j\omega C} + \frac{1}{j\omega C_\mathrm{c}} = j\frac{\omega(C+C_\mathrm{c})-\frac{1}{\omega L}}{\frac{C_\mathrm{c}}{L}+\omega^2 CC_\mathrm{c}}$, meaning that $Z_{in} = 0$ for $\omega_0 = \frac{1}{\sqrt{L(C+C_\mathrm{c})}}$ and $|Z_{in}| = \infty$ for $\omega_1 = \frac{1}{\sqrt{LC}}$. Thus the coupling capacitance led to the occurance of a resonance at $\omega_0$ with minimal input impedance. $Z_\mathrm{eff}$ as defined in (2.13) and (2.14) can be now written as

$$Z_\mathrm{eff} = Z_\mathrm{box}||Z_0 = \frac{1}{\frac{1}{Z_\mathrm{box}} + \frac{1}{Z_0}} \ , \tag{2.21}$$

Where the || sign denotes that two impedances are shunted. We see from (2.21) that $Z_\mathrm{eff}(\omega_0) = 0$ and $Z_\mathrm{eff}(\omega_1) = Z_0$. From (2.14) follows that $S_{21}(\omega_0) = 0$ and $S_{21}(\omega_1) = 1$. It is $\omega_1 > \omega_0$ and $|S_{21}| < 1$ for $0 < \omega < \omega_0$, therefore $S_{21}$ is assymetric around the resonance. The scattering parameters at any frequency can be calculated from (2.13) and (2.14). Fig. 2.11 shows scattering parameters simulated by Sonnet and calculated with (2.23) in comparison.

$$S_{11} = \frac{C_c\omega(1-CL\omega^2)Z_0}{2j(1-(C+C_c)L\omega^2) - C_c\omega(1-CL\omega^2)Z_0} \tag{2.22}$$

$$S_{21} = \frac{2j(1-(C+C_c)L\omega^2)}{2j(1-(C+C_c)L\omega^2) - C_c\omega(1-CL\omega^2)Z_0} \tag{2.23}$$

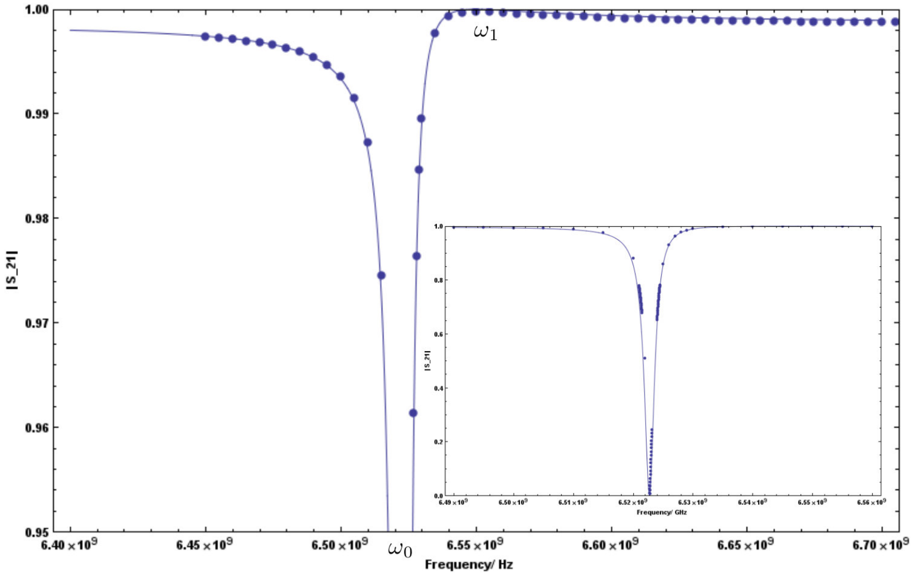


Figure 2.11: Typical $|S_{21}|$ values deliverd by a Sonnet simulation and the fitted $|S_{21}|$-curve of the lumped elements model. The large figure shows the assymetric behavior at $|S_{21}| \approx 1$ due to the capacitive coupling, and the smaller figure shows the whole resonance. At $\omega_0$ $|S_{21}|$ vanishes, whereas at $\omega_1$ $|S_{21}| = 1$.

The minimum at $\omega_0$ in Fig. 2.11 implies, that around this frequency $Z_{\text{eff}}$, representing the coupled resonator, can be approximated by the impedance of a series RLC. In fact Taylor expanding $Z_{\text{eff}}$ gives

$$Z_{\text{eff}} \approx j\,2\frac{(C+C_c)^2}{C_c^2}L\Delta\omega + \mathcal{O}(\Delta\omega^2)\,, \tag{2.24}$$

which can be written in a form similar to (2.16) by defining $L_{\text{eff}} = \frac{(C+C_c)^2}{C_c^2}L$.

## 2.5 Determinating Quality Factors from Simulated Data

The results of preceding analysis are useful for determinating quality factors of spiral resonators from data obtained by Sonnet simulations.

### 2.5.1 The -3 dB Method

We first show that a statement resembling (2.17) is valid for our capacitively coupled resonators[7]. We will, however, concider the absolute value of scattering parameter $|S21|$ instead of the input impedance, since simulation data is delivered in form of scattering paramenters. The coupling quality factor at frequency $\omega_0 = \frac{1}{\sqrt{(C+C_c)L}}$ can be calculated using the lumped element model (Fig. 2.13) and is given by

$$Q_c = \omega_0\frac{W_m + W_e}{P_l} = \omega_0\frac{\frac{|V_C|^2}{4\omega_0^2 L} + \frac{1}{4}|V_C|^2 C + \frac{1}{4}|V_{C_c}|^2 C_c}{|V_{Z_0}|^2/Z_0} = 2\frac{(C+C_c)\sqrt{(C+C_c)L}}{C_c^2 Z_0}\,. \tag{2.25}$$

From (2.14) and (2.21) it is $|S_{21}|^2 = \left[1 + \frac{C_c^2\omega^2(CL\omega^2-1)^2 Z_0^2}{4((C+C_c)L\omega^2-1)^2}\right]^{-1} = \left[1+\frac{1}{4}Y\right]^{-1}$. Let $BW_\omega$ be the width of $|S_{21}|$-curve at the point where $Q \approx \frac{\omega_0}{BW_\omega}$. Approximating $\omega^2 = (\omega_0+\Delta\omega)^2 \approx \omega_0^2 + 2\omega_0\Delta\omega$

[7] This is reasonable because the coupled resonator, in contrary to the uncoupled spiral, can be approximated as series RLC, as shown in 2.24.

for a small $\Delta\omega = \frac{1}{2}BW_\omega$ we can write $Y = \frac{(QC_c^2Z_0 - CC_cZ_0)^2(QC_c^2Z_0 + C_c^2Z_0)}{\frac{1}{4}Q^3C_c^6Z_0^3} = 4\Big(1 + \mathcal{O}\big(\frac{1}{Q}\big)\Big)$, which is effectively 4 for a big Q. Thus $|S21| = \frac{1}{\sqrt{2}}$ when $Q \approx \frac{\omega_0}{BW_\omega}$

Since $Q \approx \frac{\omega_0}{BW_\omega}$ at $|S21| = \frac{1}{\sqrt{2}}$ one can determine Q by measuring $BW_\omega$ and resonance frequency $\omega_0$. In case scattering parameters are given in dB, $|S_{21}|^2 = \frac{1}{2}$ corresponds $|S_{21}| = -3dB$. This method however often is tedious because $BW_\omega$ can be measured properly only after performing several "zoom-in" simulations.

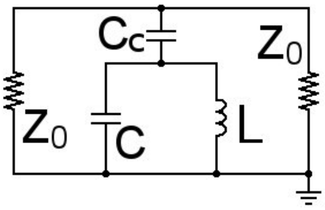


Figure 2.12: Model used for calculating the Q factor. The calculation implies that voltage is applied at capacitance C at t = 0, power passing through $C_c$ at t > 0 is dissipated.

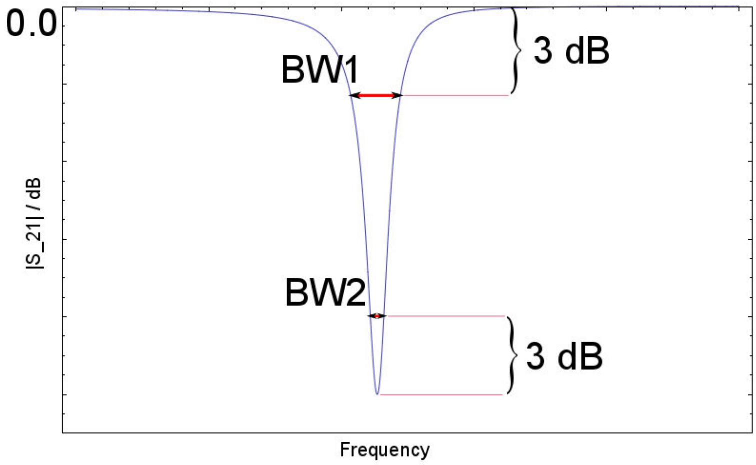


Figure 2.13: Measuring the the width of the resonance allows to determine the quality factors of a resonator. Measuring the width 3dB below $|S_{21}| = 1$ gives the overall, loaded $Q$. It is $Q = \frac{\omega_0}{\mathrm{BW}_1}$, where $\omega_0$ is the resonance frequency and BW the width. Through measuring the width 3dB above the resonance minimum one obtains the internal quality factor $Q_i = \frac{\omega_0}{\mathrm{BW}_2}$ (see 2.3.1). Since in this chapter we are considering a lossless resonator, power only dissipates through the coupling to cirquitry and the quality factor corresponding to $\mathrm{BW}_1$ is the coupling quality factor $Q_c = Q$ (see (2.20)).

### 2.5.2 Determination of Q through linearization of $S_{21}$

Near $\omega_0$ $|S_{21}|$ behaves linear and can be approximated by

$$|S_{21}| = 4\frac{(C+C_c)^2 L}{C2^2 Z_0}\Delta\omega + \mathcal{O}(\Delta\omega^2) = 2Q\frac{\Delta\omega}{\omega_0} + \mathcal{O}(\Delta\omega^2)\,. \tag{2.26}$$

If therefore a simulation delivers some $|S_{21}|$-values near zero, the Q factor can be determined from (2.26).

### 2.5.3 Determination of Q Using a Third Port

Additionally, as shown in Ref. [17], Q can be determined using a third port directly attached to the resonating part of the circuit (Fig. 2.14). The third port allows to measure the resonator's input impedance. Although in simulations resonators are assumed lossless, their input impedance $Z_{in}$ can be approximated by that of parallel or series RLC with finite R due to energy dissipation through their coupling to feedlines. Ref. [17] conciders the series RLC case, where from (2.16) one sees immediately that $\Re(Z_{in}) = R$ and $\frac{d\Im(Z_{in})}{d\omega} = \frac{2RQ}{\omega_0}$. This is not obvious for the parallel RLC circuit representing a resonating spiral, however Taylor expanding (2.18) around $\omega_0$ shows that here $Z_{in} = R - j\frac{2RQ}{\omega_0}\Delta\omega$. In both cases Q can be determined from $\Re(Z_{in})$ and the slope $S = \frac{d\Im(Z_{in})}{d\omega}$ at resonance.

$$R = \Re(Z_{in}(\omega_0)) \tag{2.27}$$

$$Q = \left|\frac{S\omega_0}{2R}\right|. \tag{2.28}$$

All three methods were used during this work. If carried out properly the results of all three methods are in good agreement with each other (see Table 2.1).

| Method | $Q_c$ |
|---|---|
| -3 dB | $2330 \pm 30$ |
| Linearization | $2324 \pm 5$ |
| Third port | $2330 \pm 5$ |

Table 2.1: The quality factor of a resonator at 6.52 GHz was determined using the three described methods. The results were in good agreement.

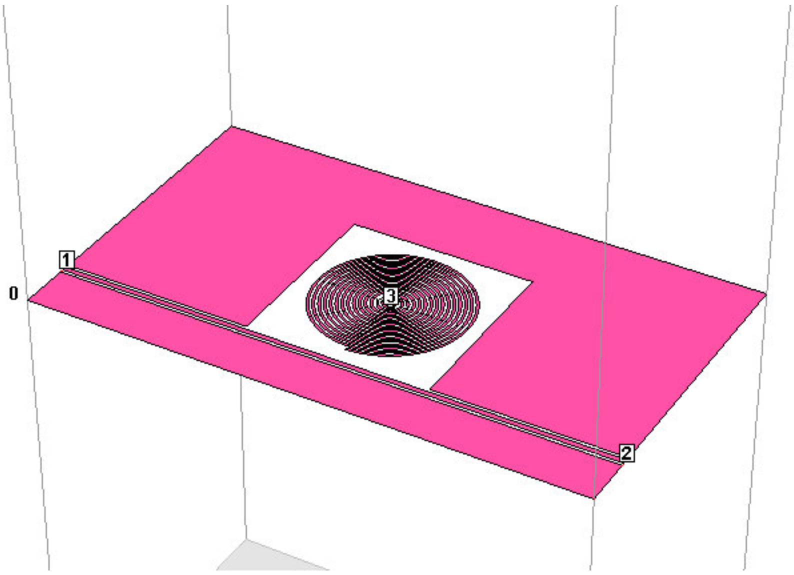


Figure 2.14: Geometry of a Sonnet simulation using three ports.

# Chapter 3

# Design and Simulation of Spiral Resonators

## 3.1 Spiral Design

Two types of resonating spirals were chosen to be investigated during this work. First a simple Archimedean and second a double wound spiral (Fig. 3.1). The layouts were created with LEdit [18], a programm commonly used for designing MEMS, which allows to generate circuit geometry from C++ code. To parameterize the Archimedean spiral the formula

$$\vec{r}(t) = R(t) \begin{pmatrix} \cos(\omega t) \\ \sin(\omega t) \end{pmatrix} \tag{3.1}$$

was used. R(t) is a function linear in t. Through a convenient choice of R(t) and $\omega$, depending on the width of spiral loops as well as on outer and inner radii, one obtains a spiral with a given number of loops n. Parameters used to describe the spirals are listed and explained in Fig. 3.2. Double wound spirals were constructed out of two Archimedean spirals, whose centers were shifted against each other and connected with two half open toruses.

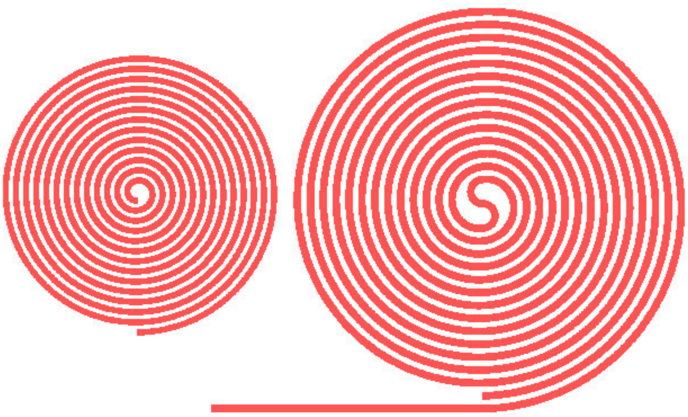

Figure 3.1: Two types of spiral resonators were simulated: a simple Archimedean spiral and a double wound spiral as seen on the right.

In total 32 resonators of different resonant frequencies, quality factors and widths of spiral loops were designed. The resonators were distributed on four chips, with eight resonators on each.

All resonators on one chip differ in frequencies but are of the same type (simple or double wound). Four of the resonators on each chip have a high coupling Q (order of $10^5$) and four have a low one (order of $10^3$). Table 3.1 lists all the resonators and chips.

| Chip | Resonant frequency | Type of spiral | Width of spiral loops | $Q_c$ |
|---|---|---|---|---|
| SPIRAL_S_1_1 | | | | |
| | 5 GHz | simple Archimedean | 1µm | $\approx 10^3$ |
| | 6 GHz | " | " | " |
| | 7 GHz | " | " | " |
| | 8 GHz | " | " | " |
| | 5.25 GHz | " | " | $\approx 10^5$ |
| | 6.25 GHz | " | " | " |
| | 7.25 GHz | " | " | " |
| | 8.25 GHz | " | " | " |
| SPIRAL_S_5_5 | | | | |
| | 5 GHz | simple Archimedean | 5µm | $\approx 10^3$ |
| | 6 GHz | " | " | " |
| | 7 GHz | " | " | " |
| | 8 GHz | " | " | " |
| | 5.25 GHz | " | " | $\approx 10^5$ |
| | 6.25 GHz | " | " | " |
| | 7.25 GHz | " | " | " |
| | 8.25 GHz | " | " | " |
| SPIRAL_D_1_1 | | | | |
| | 5 GHz | double wound | 1µm | $\approx 10^3$ |
| | 6 GHz | " | " | " |
| | 7 GHz | " | " | " |
| | 8 GHz | " | " | " |
| | 5.25 GHz | " | " | $\approx 10^5$ |
| | 6.25 GHz | " | " | " |
| | 7.25 GHz | " | " | " |
| | 8.25 GHz | " | " | " |
| SPIRAL_D_5_5 | | | | |
| | 5 GHz | double wound | 5µm | $\approx 10^3$ |
| | 6 GHz | " | " | " |
| | 7 GHz | " | " | " |
| | 8 GHz | " | " | " |
| | 5.25 GHz | " | " | $\approx 10^5$ |
| | 6.25 GHz | " | " | " |
| | 7.25 GHz | " | " | " |
| | 8.25 GHz | " | " | " |

Table 3.1: Table of the 32 designed resonators and their characteristics. The chip names are as written on the chips themselves; S/D meaning simple or double, 1_1 and 5_5 indicating the width of spiral loops and distance between loops in µm.

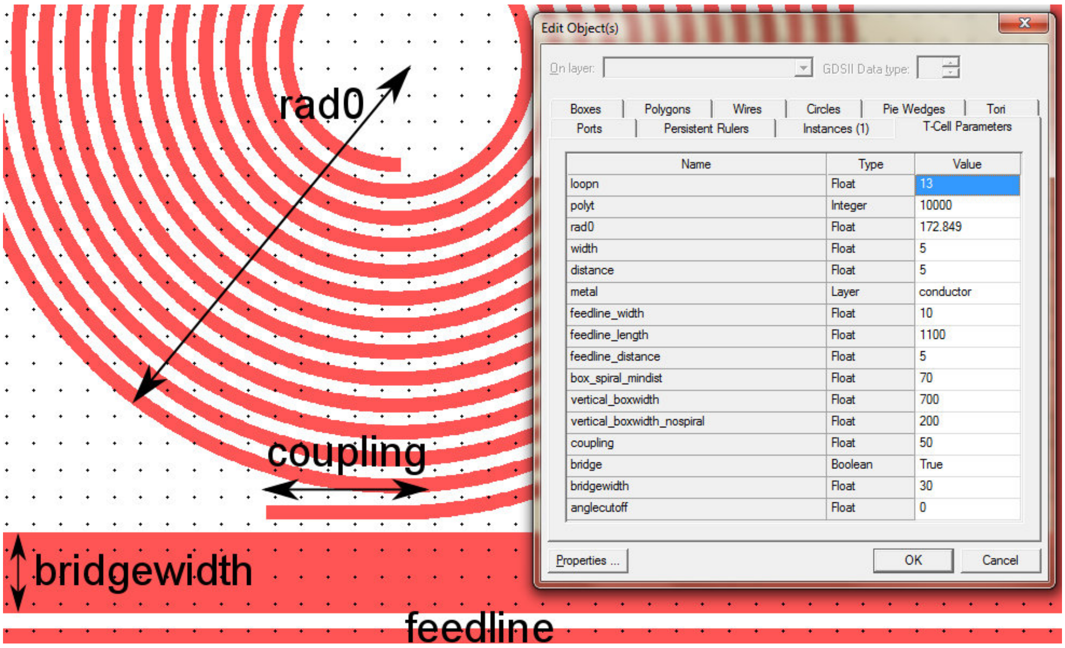


Figure 3.2: Parameters used to specify a spiral resonator's geometry. loopn: number of loops, polyt: number of vertices of the spiral polygon. rad0: outer radius, width: width of spiral loops, distance: distance between spiral loops. feedline_distance: distance between spiral coupling and feedline or bridge. coupling: length of spiral's capacitive coupling. bridge: whether a grounded bridge between feedline and spiral is placed to achieve a higher $Q_c$. anglecutoff: angle to be cut off at the inner end of the spiral to fine tune the resonant frequency.

The quality factor $Q_c$ as calculated from the lumped elements model (see 2.5) is given by

$$Q_c = 2\frac{(C+C_c)\sqrt{(C+C_c)L}}{C_c^2 Z_0}\,, \tag{3.2}$$

meaning that we can adjust $Q_c$ by varying the coupling capacity $C_c$. To do so it is possible to vary the distance between coupling and feedline $d$ or the length of the couling $l$ - analogous to a parallel-plate capacitor. Aditionally to achieve a higher $Q_c$ a grounded bridge of width $w$ can be placed between coupling and feedline (for typical values of $d$, $l$ and $w$ see table 3.1). In case of our resonators $C_c$ was adjusted once at a certain frequency for a certain type of spiral (simple or double wound design, 5 or 1 µm loop width, coupling strength) and then kept while varying frequency. Thus the $Q_c$ of resonators with same coupling geometry but different frequencies varies by a factor of two to three, which is not surprising, since, to vary the frequency from 5GHz to 8GHz the resonator's geometry, i.e. C and L have to be changed.

| Type of Resonator | Resesonance frequency /GHz | Coupling length /μm | $Q_c$ | Width of grounded bridge /μm |
|---|---|---|---|---|
| Simple Archimedean | 8.2 | 6 | 670 | 0 |
| Simple Archimedean | 8.2 | 26 | 10500 | 15 |
| Double wound | 8.3 | 1 | 5000 | 0 |
| Double wound | 8.3 | 8 | 11000 | 1 |

Table 3.2: Data on coupling length, width of grounded bridge between feedline and coupling as well as distance between feedline and coupling for simple Archimedean and double wound types of resonators with a loop width of 1μm.

Altering the radius as well as the number of loops and thereby it's length changes the resonance frequency of a spiral resonator. Facing the task of designing 32 resonators with given frequencies it seems reasonable to change only one of the many spiral parameters from Fig. 3.2. The decision was made to let the number of loops constant for a certain type of spiral and to alter the frequency by changing the outer radius. Since the width of spiral loops was fixed to 1 or 5 μm altering the outer radius automatically leads to an altered inner radius, which is not an independent parameter in our design (see Fig. 3.3).

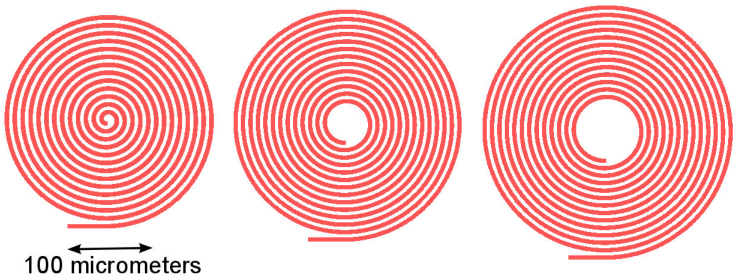


Figure 3.3: To vary the resonant frequencies, outer radii of the spirals were changed, whereas the number of loops was held constant. The figure shows resonators at 8.25, 6.25 and 5.25 GHz.

Finally, for each type of spiral, frequencies were adjusted in the same way. Four outer radii were chosen by eye, simulated and than, through an interpolation of obtained results, radii corresponding to the required frequencies were calculated. As an example we show how the frequencies of the four double wound resonators with a loop width of 5μm and $Q_c$of order $10^5$ were adjusted. Here simulations yielded in the results shown in table 3.3.

| Outer radius /μm | Resonant frequency /GHz |
|---|---|
| 159 | 8.36 |
| 180 | 6.56 |
| 198 | 5.53 |
| 212 | 4.93 |

Table 3.3: Results of simulations of four double wound resonators with a loop width of 5μm and different outer radii.

This data was interpolated with a polynomial of fourth degree:

$$r_{outer} = 509\mu\text{m} - 106\frac{\mu\text{m}}{\text{GHz}}\nu + 11.7\frac{\mu\text{m}}{\text{GHz}^2}\nu^2 - 0.478\frac{\mu\text{m}}{\text{GHz}^3}\nu^3\,, \tag{3.3}$$

which allows to calculate radii leading to needed resonance frequencies (table 3.4).

| Outer radius /µm | Resonant frequency /GHz |
|---|---|
| 204 | 5.25 |
| 184 | 6.25 |
| 170 | 7.25 |
| 159 | 8.25 |

Table 3.4: Calculated outer radii of four double wound resonators with a loop width of 5µm and $Q_c$of order $10^5$.

Figure 3.4 shows the simulated frequencies and the interpolation polynomial.

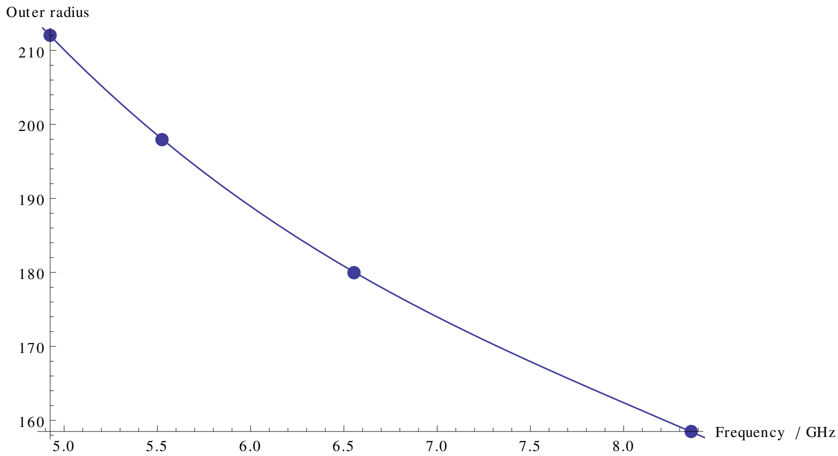


Figure 3.4: Outer radii in µm and resonance frequencies of four double wound spirals. Simulated frequencies and the interpolation polynomial used to determine radii corresponding to given resonance frequencies.

After designing the resonators in the manner described above they were distributed on chips according to table 3.1. A chip is shown in Fig. 3.6. Although our resonators nominally are measured at zero magnetic field, to avoid energy dissipation due to Abrikosov vortices in case of some residual magnetic field, flux traps were placed on the chips as suggested by Ref. [19]. The traps consist of rectangular, 10x10 $\mu m^2$ large holes in the superconducting film and were distributed 10µm apart from each other over the whole surface of the chip. No flux traps were placed on the spiral itself and the feedline. A strip of 5µm width around the edges of feedline and resonator box was kept flux trap free to avoid influence on quality factors and resonance frequencies (Fig. 3.5).

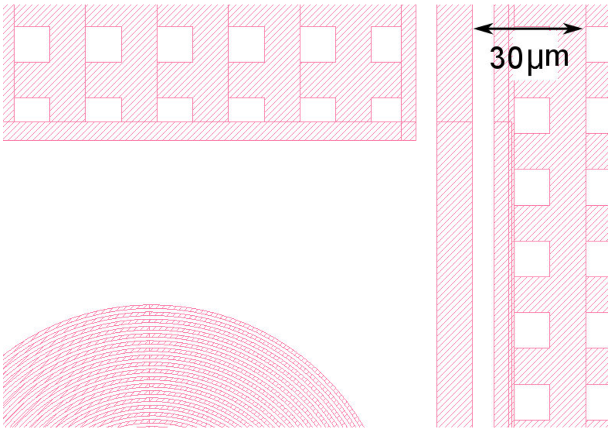


Figure 3.5: Rectangular nonconducting flux traps were placed on the chip's surface to lower the energy losses due to Abrikosov vortices. The flux traps are 10x10 µm$^2$ in size.

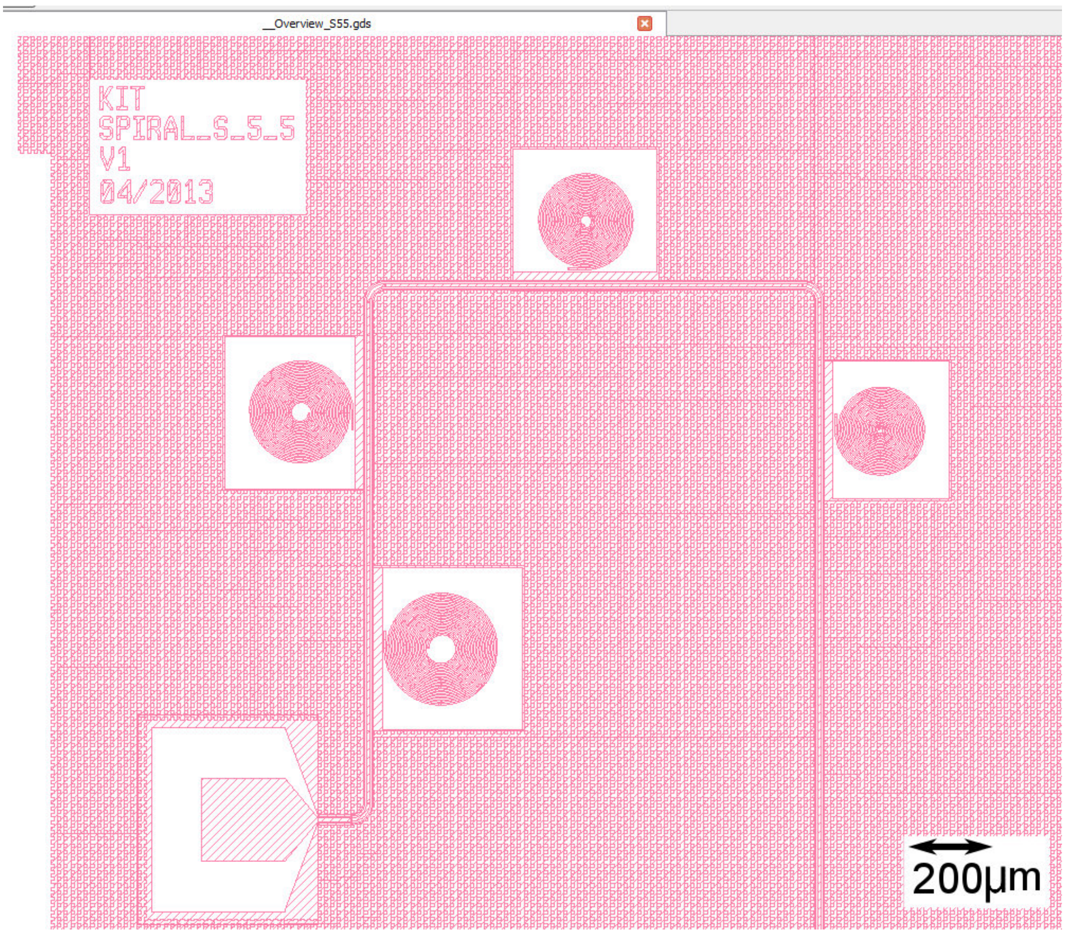


Figure 3.6: Part of a chip consisting of launcher and four resonators. Eight resonators of the same kind were placed on every chip.

| Type | Radii of 5.0 GHz resonators | Radii of 8.0 GHz resonators |
|---|---|---|
| Simple_1_1 | 78 µm | 62 µm |
| Double_1_1 | 91 µm | 70 µm |
| Simple_5_5 | 178 µm | 140 µm |
| Double_5_5 | 210 µm | 161 µm |

Table 3.5: Radii of smallest and largest resonators of every type.

## 3.2 Simulation of Resonators

To determine the resonance frequency and quality factor of designed resonators the spirals were simulated with Sonnet [20]. Sonnet is a commercial software, which allows simulations of planar circuits or antennas at high frequencies. As described in the previous section, in order to obtain precise resonance frequencies the parameters of a spiral were changed by eye and then simulation results were interpolated. Simulations were carried out with the two port geometry shown in figure 3.7, employing a third port for determining $Q_c$ if necessary. The flux traps were not simulated due to memory constrains, however the grounded planes around spiral and feedline were included. As the feedline width was chosen to be 10µm, the distance between feedline and grounded box was fixed to 6µm ensuring a characteristic transmission line impedance of 50Ω to avoid wave reflection at the ports.

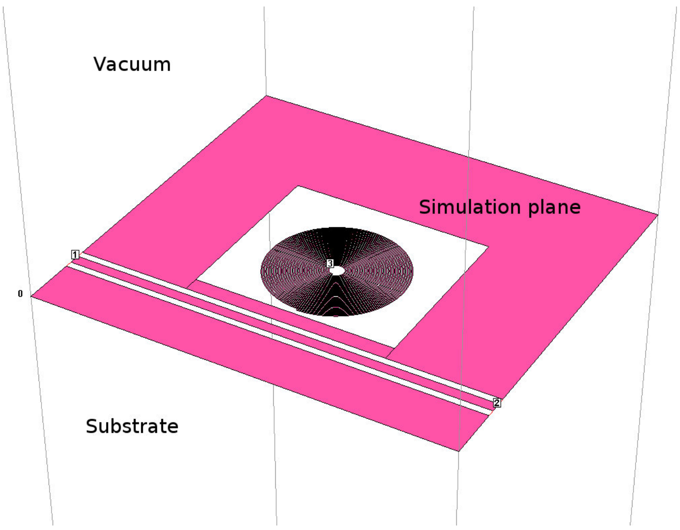


Figure 3.7: Geometry of Sonnet simulations. Simulation plane with spiral and grounded box consisting of an ideal conductor. Vacuum ($\epsilon_r = 1$) above and silicon ($\epsilon_r = 11$) below the simulation plane.

Silicon is used as substrate for resonator chips, so a dielectric constant $\epsilon = 11$ was chosen as material parameter for the layer below and $\epsilon = 1$ for the layer above the superconducting surface (vacuum). The thickness of both layers was chosen to be 1000µm (see Fig. 3.7). All conducting parts were simulated as ideal conductors with zero resistance; dielectric losses were neglected, too.

The results of a simulation are given in terms of scattering parameters $S_{ij}$ or in terms of impedances. Being at the minimum of transmission the resonance frequency can be directly seen from the $S_{21}$ data. $Q_c$ factors were determined using methods described in the resonator theory chapter. The duration of a simulation strongly depends on the quality factor of a simulated resonator. For a high $Q_c$ resonator it is more difficult to obtain an accurate resonance curve, since the curve is narrow and demands a high resolution in frequency space.

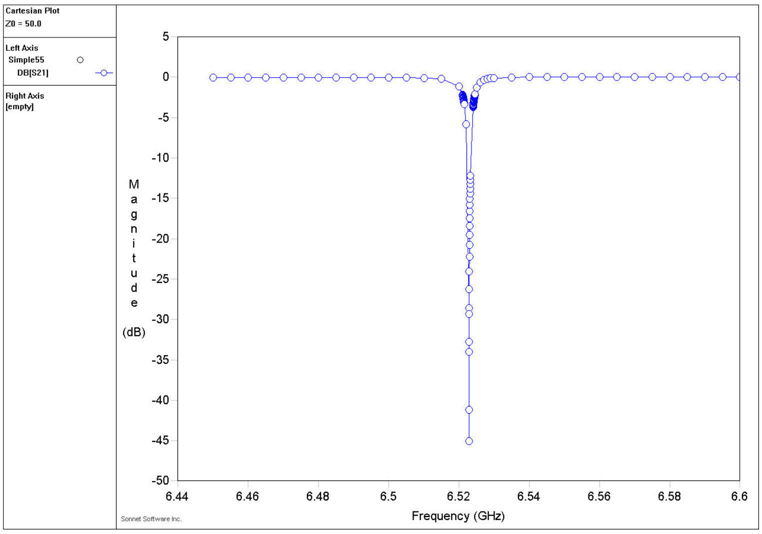


Figure 3.8: A typical $S_{21}$ curve of a resonator as shown in Fig 3.7 delivered by Sonnet. At resonance S21 is minimal.

It was found that a double wound spiral has a higher resonance frequency and a considerably higher $Q_c$than a simple Archimedean spiral of same radius and same geometrical coupling properties (see table 3.6).

| | Radius /µm | Length /µm | Frequency /GHz | Q |
|---|---|---|---|---|
| Simple spiral | 155 | 7479 | 6.52 | 2330 |
| Double wound spiral | 155 | 7060 | 9.0242 | 16700 |
| Double wound spiral | 159.6 | 7478 | 8.49 | 18400 |

Table 3.6: Comparison of resonant frequencies and quality falctors of simple and double wound spirals of same length or radius. Double wound spirals have a higher $Q_c$and a higher frequency.

This phenomenon can be understood qualitatively considering that the inductance of a double wound spiral is lower than that of a simple spiral, because the current along a double wound spiral has to flow inward and then outward, so that the magnetic fields created by the currents partially annihilate each other. Since $\Phi = LI$ a lower magnetic flux means a lower inductance. The resonance frequency of an LC resonator is given by $\omega_0 = 1/\sqrt{LC}$ so that a lower inductance leads to a higher resonance frequency.

In an open circuited $\lambda/2$ TL resonator (see Fig. 3.9) the voltage is maximal at one and minimal at the other end. In case of the double wound spiral voltage difference along the spiral induced by the feedline is small, because both ends of the spiral are at nearly the same distance from the feedline. In case of the simple spiral one end of the spiral is much nearer to the feedline than the other, hence the induced voltage is higher, resulting - together with the larger inductance - in a lower quality factor.

### 3.2.1 Current Density and Field Distribution in Simple Archimedean and Double Wound Spirals

As described in Chapter 2.4 the spiral resonator should qualitatively behave as an open circuited $\lambda/2$ TL resonator. Figure 3.9 shows that at the fundamental resonant frequency ($n = 1$) the absolute voltage value should be maximal at the ends of the TL. This implies that the current density is minimal at the ends and maximal in the middle (at $l/2$) of the resonator. In fact simulations confirmed that this is the case. Figures 3.10 and 3.11 show the current destributions along simple and double wound spirals, figures 3.12 and 3.13 show the corresponding field distributions[1].

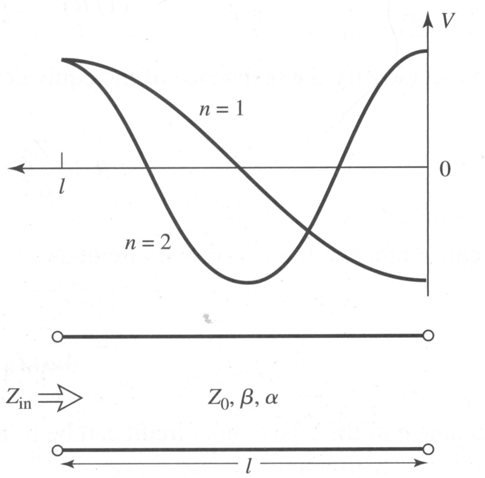


Figure 3.9: Voltage distribution along an open circuited $\lambda/2$ TL resonator, which can be used to develop a qualitative understanding of the behaviour of the spiral resonator. n=1 stands for the fundamental frequency and n=2 for the second harmonic. The resonator has a characteristic impedance $Z_0 = \alpha + j\beta$. Note that the current density is minimal at the TL's ends. ([?],S.276)

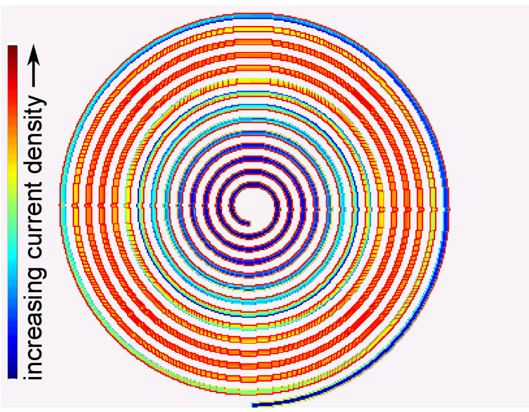


Figure 3.10: Current destribution along a simple Archimedean spiral at the fundamental resonance frequency. As expected from comparison with the open circuited $\lambda/2$ TL resonator the current density is minimal at the spiral's ends. Simulation was performed with Sonnet.

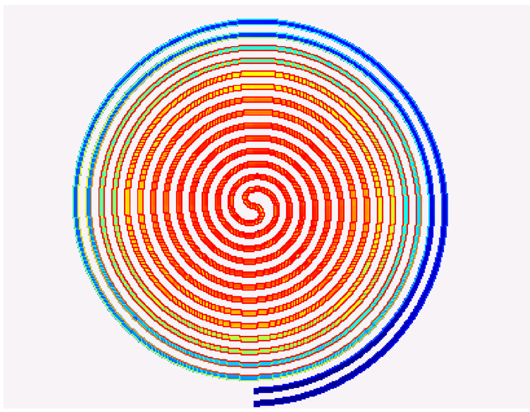

Figure 3.11: Current destribution along a double wound spiral at the fundamental resonance frequency. As expected from comparison with the open circuited $\lambda/2$ TL resonator the current density is minimal at the spiral's ends. Simulation was performed with Sonnet.

[1]Since Sonnet is designed for planar simulations, only the field component parallel to the spiral plane could be simulated. For doing so a so called sense metal plane of high reactance was placed above the resonator. The simulated current distribution along the sense metal plane is, by Ohms law $E = \sigma j$, proportional to the field strength.

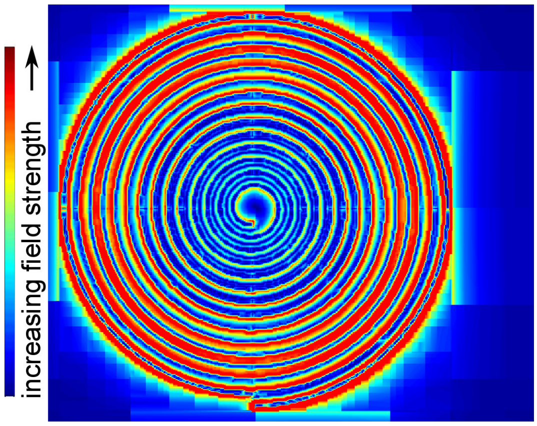


Figure 3.12: Electric field destribution of a simple spiral resonator. The field is maximal at both ends of the spiral. Note that Sonnet is only able to simulate the field component parallel to the spiral plane. The field is simulated by calculating the current destribution of sense metal plane above the resonator, hence the absolute values in this diagramm are not of particular interest.

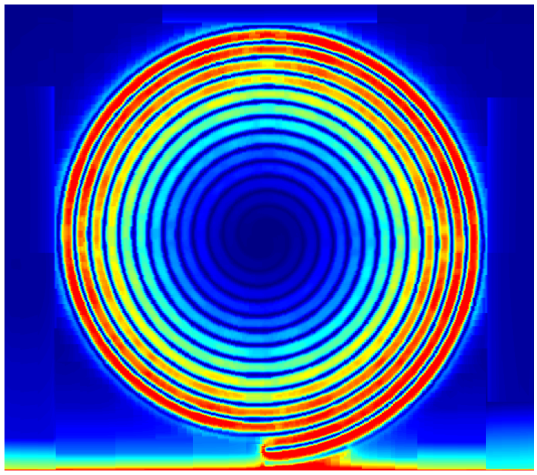

Figure 3.13: Electric field destribution of a double wound spiral resonator. The field is maximal at both ends of the spiral. Note that Sonnet is only able to simulate the field component parallel to the spiral plane.

# Chapter 4

# Measurements

One of the four chip designs was measured at 4.2 K and below. The measured chip contained double wound spiral resonators of 5 µm loop width. Resonances were observed and internal as well as coupling quality factors determined.

## 4.1 Measurement Setup

### 4.1.1 Sample Chip

Chip SPIRAL_D_5_5 (see 3.1), containing four strongly coupled ($Q_C$ of order of $10^3$) and four weakly coupled ($Q_C$ of order of $10^5$) double wound spiral resonators was measured. The chip was fabricated using intrinsic Si as substrate on which a 60 nm thick intrinsic NbN superconducting film was sputtered. The NbN film was found to have a critical temperature of 9.25 K[1]. Figures 4.1 and 4.2 show a part of the chip and a single double wound resonator.

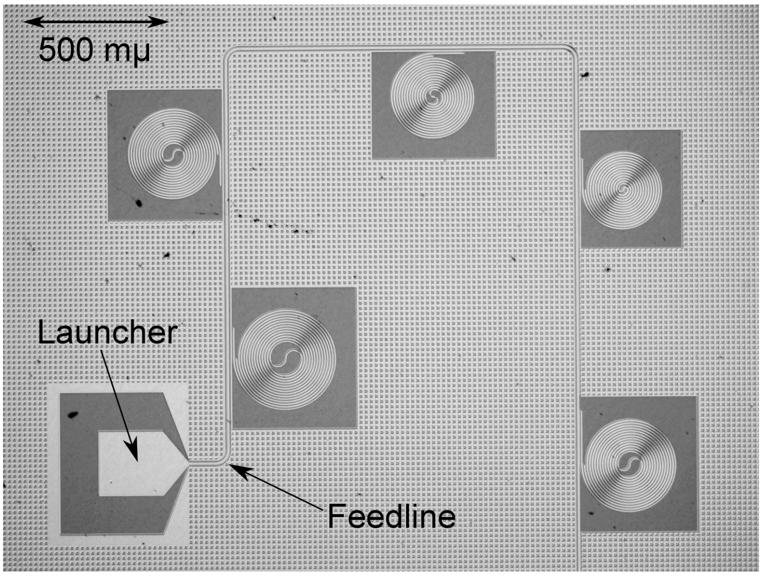


Figure 4.1: Microscope image of a part of the fabricated SPIRAL_D_5_5 chip with launcher attached to feedline and five double wound spiral resonators of different frequencies along the feedline.

[1]Tobias Bier by private communivation.

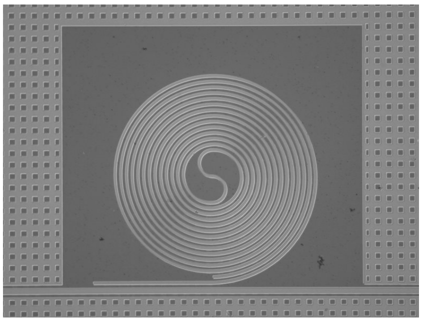

Figure 4.2: A fabricated double wound strongly coupled spiral resonator at 6 GHz. Fluxtraps, 10 x 10 $\mu m^2$ in size, were placed on the groundplane.

Before measurements the protecting photoresist for dicing was removed from the chip with aceton, isopropanol and ethanol baths. Then the chip was wire-bonded to a cryostatic sample holder (see Fig. 4.3).

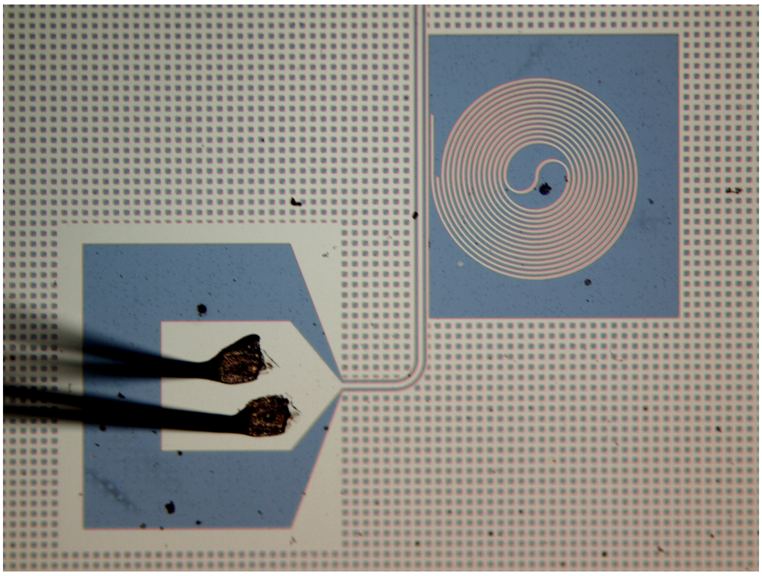

Figure 4.3: The chip's launcher bonded to the sampleholder with two bonding wires.

### 4.1.2 The Setup

After bonding the sample was attached to a dipstick (Fig. 4.4), covered with a Mu-metal magnetic shield and placed inside a helium ($^4$He) Dewar at 4.2 K. The sampleholder at the end of the dipstick was conncected to a two port Vector Network Analyzer through coaxial cables made from copper (in the upper part of the stick) and a copper-nickel alloy (used near the sampleholder to lower the thermal conductivity). To lower the transmitted power and to suppress reflexions at the connectors two 20 dB attenuators are placed in front and one 3 dB attenuator behind the sample. Additionaly the signal passes through an HEMT[2] amplifier suitable for low temperatures.

[2]Hot electron mobility transistor.

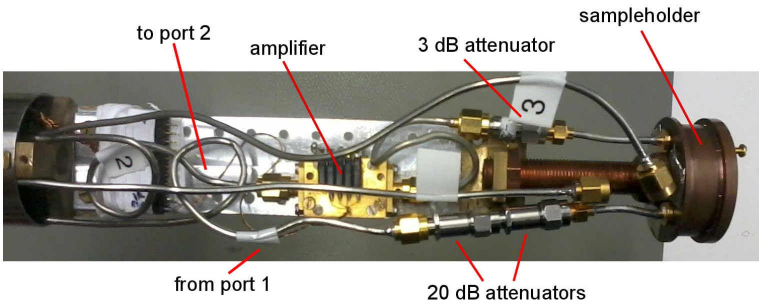


Figure 4.4: Dipstick used for measurements. To lower the transmitted power and to suppress reflexions at the connectors two 20 dB attenuators are placed in front and one 3 dB attenuator behind the sample. Additionaly the signal passes through an amplifier suitable for low temperatures.

## 4.2 Measurement Results

### 4.2.1 Overview

Four resonances were observed in the VNA range (0.4 to 8.5 GHz). Since the measurement was performed at 4.2 K which is quite high compared to the critical temperature of the superconducting NbN ($T_C = 9.25$K) we assume, that only the resonances of strongly coupled resonators were observed due to large internal losses caused by thermal quasi particles. Figure 4.5 shows the measured resonances.

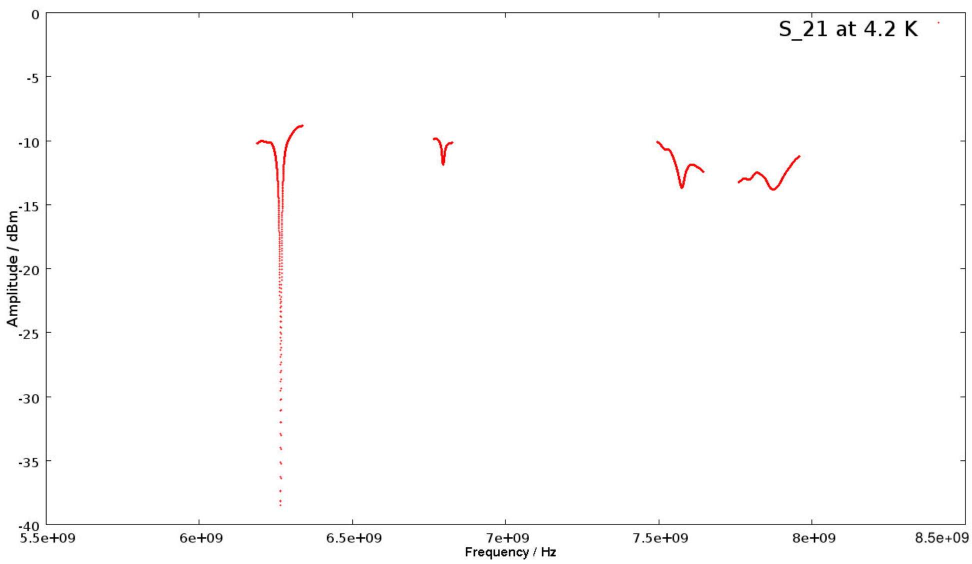


Figure 4.5: Resonances as listed in Table 4.1 measured at 4.2 K. The lowest dip, having the largest internal Q-factor, is also the deepest.

To assure that the resonances were in fact due to superconducting resonators and not part of the background their dependence on applied microwave power was tested. The resonance dips changed significantly with applied power. At high powers (0 dBm) some dips even vanished. This could be due to excitation of quasi particles, reaching of the critical current inside the resonator or simply warming up the resonator by power dissipation. The power dependence of resonances shall be discussed in detail later.

By pumping out helium gas from the Dewar the helium vapour pressure was decreased inside the Dewar and the system's overall temperature was lowered to about 3.2 K. While the temperature decreased, resonance dips became deeper and more dominant in comparison to the background (see Fig. 4.6 and Fig. 4.7), as expected from dips which are due to superconducting resonators. Table 4.1 lists the four observed resonances as well as the designed resonance frequencies. Though the observed resonances are in the same range as the designed ones it is difficult to assign the dips to certain resonators, because the shift is quite significant. For example the lowest resonator designed at 5 GHz must have been shifted more than 1 GHz up. This can be due to fabrication inaccuracies (specifically it is possible that the 5 µm widths of loops and the 5 µm distances between loops are not transfered accurately to the substrate) and / or surface contamination.

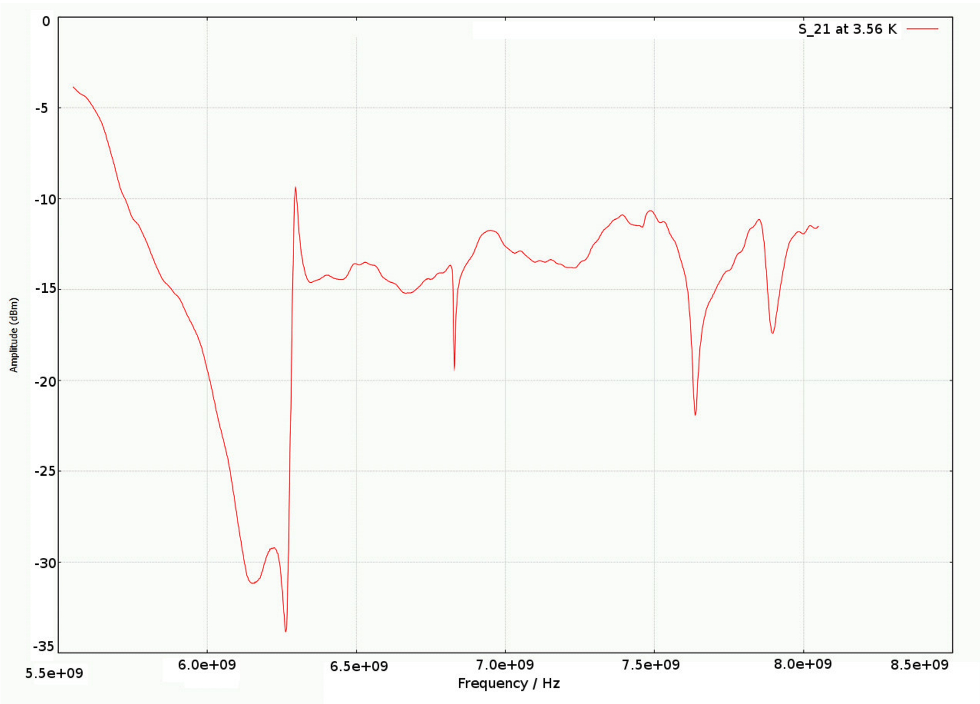


Figure 4.6: Measurement at 500 mbar vapour pressure corresponding to 3.56 K. Resonance dips become deeper at lower temperatures, internal quality factors increase, thus assuring that resonances indeed are due to by superconducting resonators. The lowest and most dominant resonance at 4.2 K is however absorbed by the background.

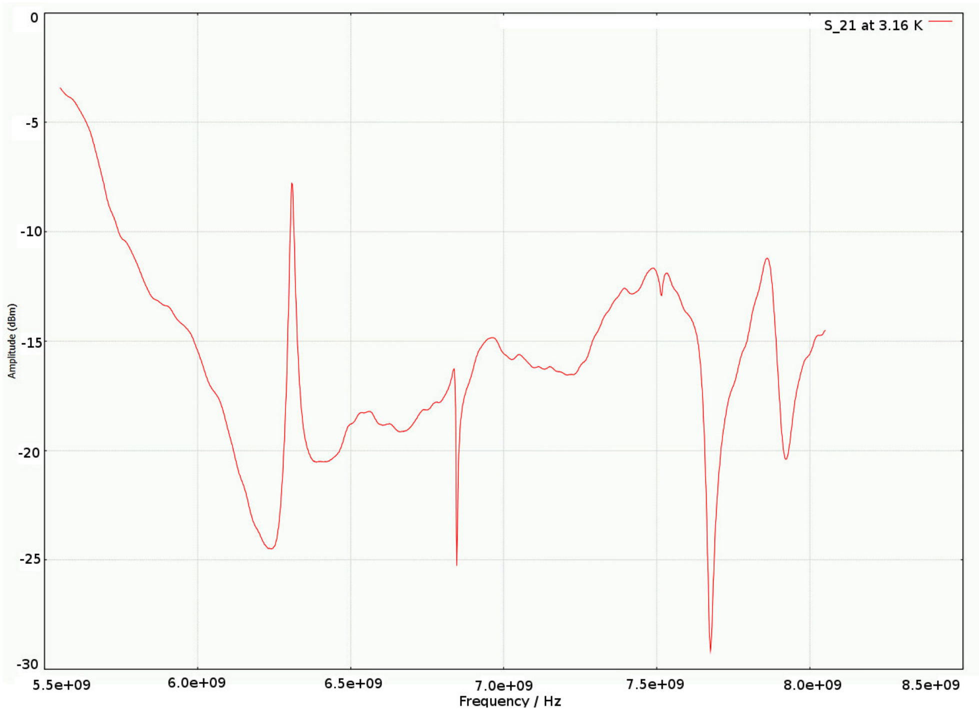


Figure 4.7: Measurement at 300 mbar vapour pressure corresponding to 3.16 K. Resonance dips become deeper at lower temperatures, internal quality factors increase, assuring that resonances indeed are due to superconducting resonators. The lowest and most dominant resonance at 4.2 K is absorbed by the background.

| Frequencies of observed resonances / Ghz | Frequencies of designed resonators / GHz |
|---|---|
| 6.26 | 5 |
| 6.79 | 6 |
| 7.57 | 7 |
| 7.86 | 8 |

Table 4.1: Frequencies of observed resonances and the frequencies of designed resonators. An assignment of observed resonances to spiral resonators is difficult because the frequency shift is significant compared to the resonator's designed difference in frequency. However the pairs 6.26 GHz - 6 GHz, 6.79 GHz - 7 GHz and 7.86 GHz - 8 GHz are in good agreement. In this case the 5 GHz resonator must have been lifted by 2.57 GHz.

### 4.2.2 Quality factors

It was discussed in 2.3.2 that given an internal quality factor $Q_\mathrm{i}$ and an external, coupling quality factor $Q_\mathrm{c}$ the overall quality factor $Q$ can be calculated as

$$\frac{1}{Q} = \frac{1}{Q_\mathrm{c}} + \frac{1}{Q_\mathrm{i}} \; . \tag{4.1}$$

The internal and external quality factors of a resonance dip can be determined by a procedure called circle fit[3] (for details see [21]). Employing this procedure we obtained all results on quality factors. The given errors are $\chi^2$ values of the fits: $\chi^2 = \sum_i \frac{(E_i - F_i)^2}{E_i}$, where $E_i$ are measured values and $F_i$ values of the fitted curve. Hence the fit delivers good results if $\chi^2$ is small. Table 4.2 shows the quality factors of three observed resonance dips[4].

| Frequency / GHz | $Q_\mathrm{i}$ / $10^3$ | $Q_\mathrm{C}$ / $10^3$ | Error of Fit | Power / dBm |
|---|---|---|---|---|
| 6.26 | 2.8 | 0.30 | $1.9 \cdot 10^-4$ | -10 |
| 6.79 | 0.80 | 3.9 | $2.3 \cdot 10^-5$ | -10 |
| 7.86 | 0.19 | 0.72 | $4.3 \cdot 10^-4$ | -30 |

Table 4.2: Internal and coupling quality factors of three resonance dips. Since $Q_\mathrm{c}$s were designed to be of the order of $10^3$ they are - with exception of the 6.79 GHz dip - lower than expected. The internal quality factors also are low, which is not surprising because the measurement was made at the comparatively high temperature of 4.2 K.

### 4.2.3 Power Dependence of Resonances

Typically the resonance dip of a superconducting resonator exhibits a dependence on the power transmitted through the circuit (chip). This can be due to excitation of quasi particles, reaching of the critical current inside the resonator or simply warming up the resonator by power dissipation.

#### The 6.26 GHz Resonance

The four resonances from Table 4.1 show a power dependence, which is most striking in case of the 6.26 GHz resonance as shown in Fig. 4.8.

[3]Because imaginary and real parts of $S_{21}$ if plotted against each other sweeping through the resonance ideally form a circle.

[4]The Q factor of the 7.57 GHz resonance was not measured because the resonance dip showed two $S_{21}$ minima (see 4.2.3).

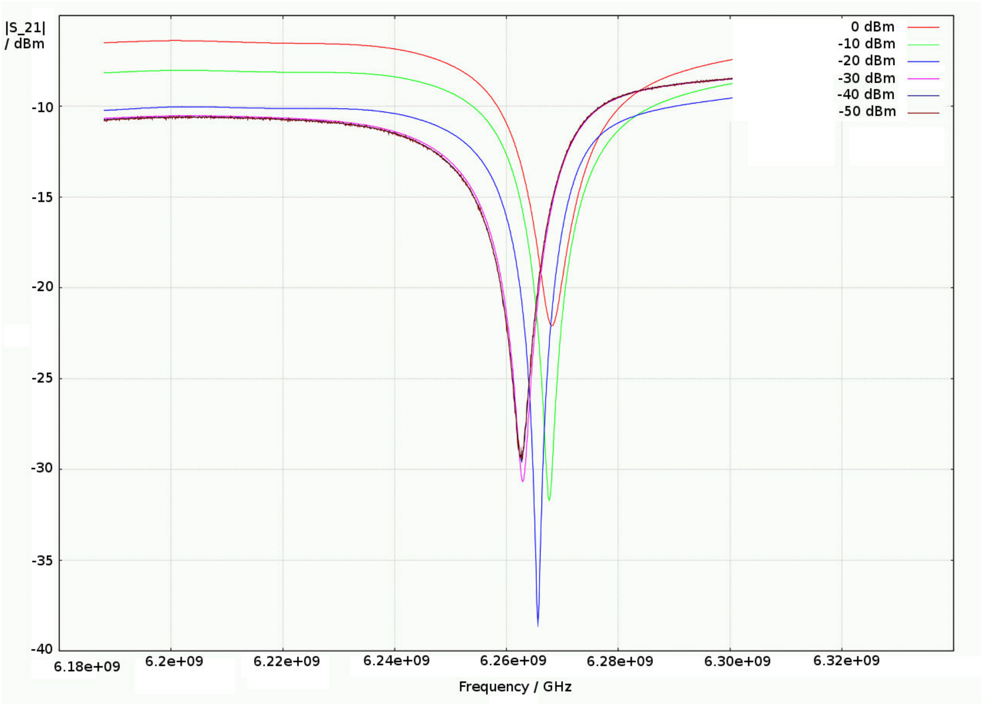


Figure 4.8: Amplitudes of the 6.26 GHz resonance at different transmission powers at 4.2 K. The resonance dip becomes deeper as power is lowered. It is deepest at -20 dBm. Also a frequency shift is observable.

As is obvious from Fig. 4.8 lowering the transmission power shifts the resonance frequency to lower frequencies. This effect is quite small ($\approx -5$MHz over the range from 0 to -50 dBm). The shift is shown seperately in Fig. 4.9. Also the quality factors of the resonator vary with frequency (see Fig. 4.10 and Table 4.3). Around -20dBm the internal quality factor is about ten times higher than at other frequencies, here we also observe that the dip is deepest (Fig. 4.9). Also the lowest internal quality factor is at 0dBm, meaning that here power dissipation inside the resonator is highest.

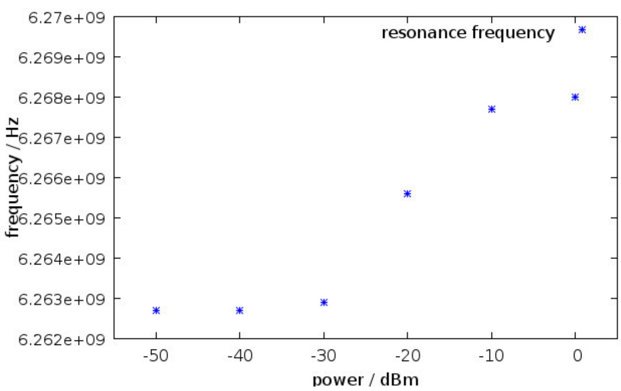


Figure 4.9: Frequency shift due to transmitted power of the 6.26 GHz resonance at 4.2 K. Frequency decreases as power is lowered. The shift is maximal around -20dBm, where the internal Q of the resonator is highest and the dip deepest.

| Power / dBm | $Q_\mathrm{i}$ / $10^3$ | $Q_\mathrm{c}$ / $10^2$ | Error of Fit |
|---|---|---|---|
| 0 | 1.3 | 3.2 | $2.3\cdot10^{-4}$ |
| -10 | 2.6 | 3.0 | $1.7\cdot10^{-4}$ |
| -17 | 8.7 | 2.8 | $2.5\cdot10^{-4}$ |
| -19 | 14 | 2.8 | $3.0\cdot10^{-4}$ |
| -20 | 28 | 2.7 | $3.1\cdot10^{-4}$ |
| -30 | 3.3 | 3.0 | $6.1\cdot10^{-4}$ |
| -40 | 2.6 | 3.2 | $6.7\cdot10^{-4}$ |
| -50 | 2.5 | 3.3 | $7.1\cdot10^{-4}$ |

Table 4.3: Power dependence of internal and coupling quality factors of the 6.26 GHz resonator. The internal quality factor shows a maximum around -20dBm. The coupling quality factor remains approximately constant. Since $Q_\mathrm{c}$ is dominated by the geometry of a resonator the observed behavior is reasonable.

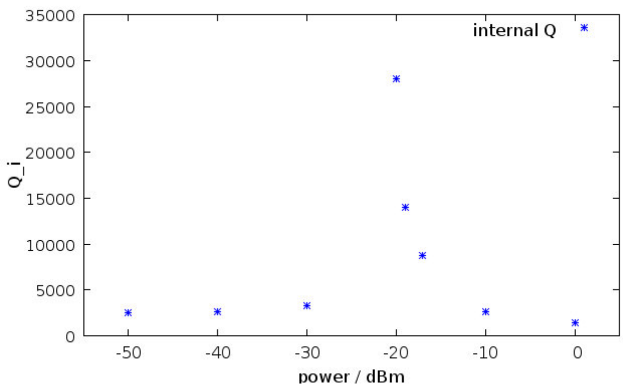


Figure 4.10: Lowering the transmitted power strongly increases the internal Q of the 6.26 GHz resonance above -20 dBm. At lowest powers Q again falls. Measurement performed at 4.2 K

### The 6.79, 7.57 and 7.86 GHz resonances

For the 6.79 GHz resonance we observe (Fig. 4.11) that the dip is becoming deeper as transmitted power is decreased. Also a slight shift from lower to higher frequencies is observable. This shift is approximately of the same magnitude as the shift of the 6.26 GHz resonator.

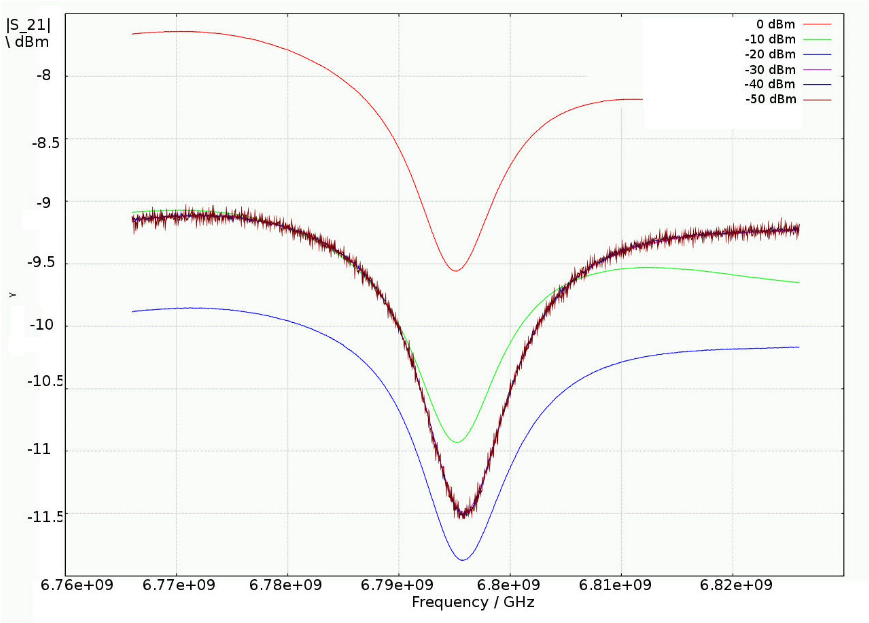


Figure 4.11: The 6.79 GHz resonance dip becomes deeper as the transmitted power is lowered. A slight frequency shift towards higher frequencies is observable. The measurement was performed at 4.2 K.

The power dependence of the 7.57 GHz resonance is pictured in Fig. 4.12. Above -10 dBm the $S_{21}$ data shows two minima: at 7.57 and 7.56 GHz. However the lower frequency minimum disappears at powers below -10 dBm, whereas the 7.57 GHz dip remains visible. A possible explanation is that one of this dips belongs to a weakly coupled resonator.

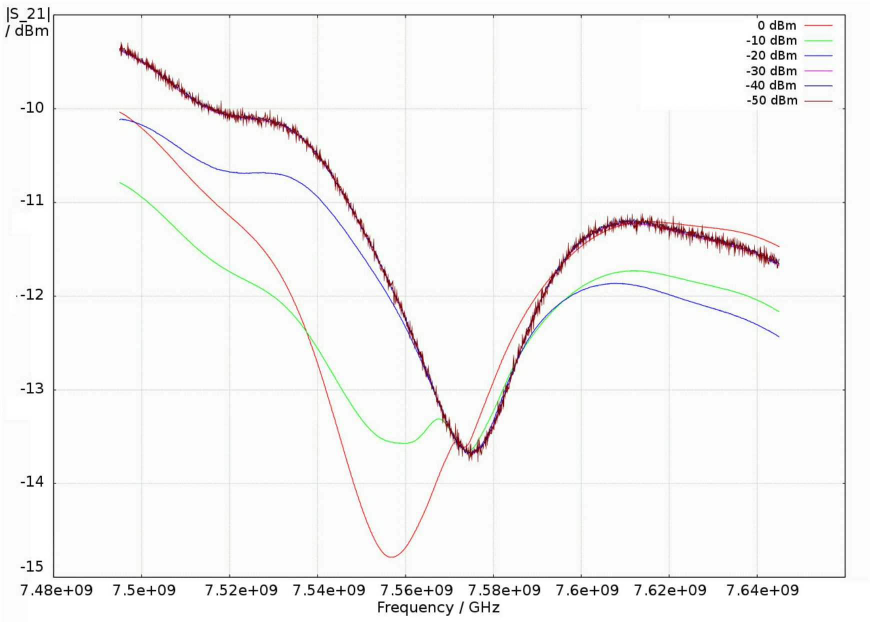


Figure 4.12: At high powers the resonance at 7.57 GHz shows two minima, however at lower powers the lower minimum disappears, while the upper minimum becomes more distinct. The measurement was performed at 4.2 K.

In case of the 7.86 GHz resonance we again see the dip becoming more distinct as the transmitted power is decreased (Fig. 4.13). Here the effect is even more striking as in case of the 6.79 GHz resonance.

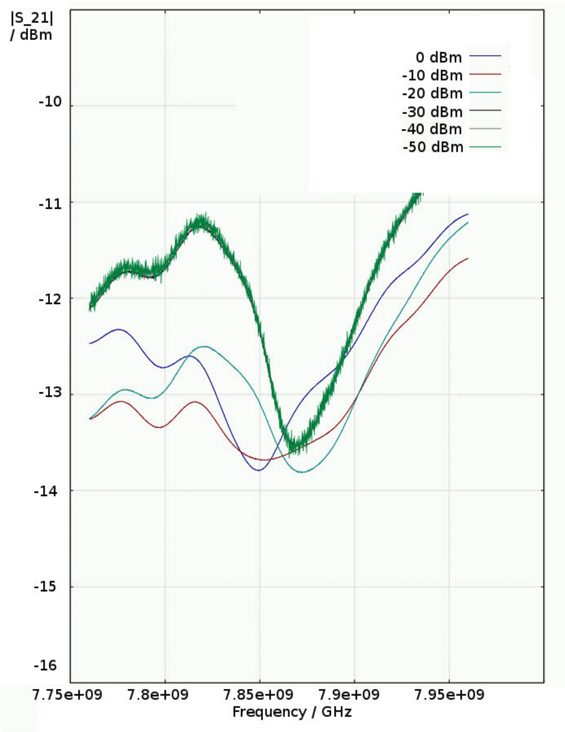


Figure 4.13: Lowering the transmitted power, we observe that the 7.86 GHz resonance dip becomes more distinct. The measurement was performed at 4.2 K.

### 4.2.4 Temperature Dependence of the Frequency and the Quality Factors of the 6.79 GHz Resonance

Lowering the vapour pressure inside the helium Dewar temperatures down to 3.2 K - corresponding a vapour pressure of 300 mbar - were achieved. As the temperature was decreasing, the dips became deeper and internal quality factors higher, also the frequencies shifted to higher values. Table 4.4 shows the temperature dependence of frequency and quality factor of the 6.79 GHz resonance.

| Vapour pressure | Temperature / K | Frequency / GHz | $Q_{\mathrm{i}}$ / $10^3$ | $Q_{\mathrm{C}}$ / $10^3$ | Error of Fit |
|---|---|---|---|---|---|
| 1000 mbar | 4.2 | 6.79 | 0.80 | 3.9 | $2.3 \cdot 10^{-5}$ |
| 700 mbar | 3.9 | 6.82 | 1.1 | 3.7 | $1.1 \cdot 10^{-4}$ |
| 300 mbar | 3.2 | 6.84 | 3.4 | 1.7 | $4.5 \cdot 10^{-3}$ |

Table 4.4: Temperature dependence of internal and coupling quality factors of the 6.79 resonance dip. Resonance frequency shifts with temperature. For dependence of temperature upon vapour pressure see Ref. [22].

# Conclusion

This thesis shows how the task of designing superconducting microwave spiral resonators was approached by means of electromagnetic simulation (using Sonnet) of created layouts (LEdit). The designed resonators were measured and found to be functional, having resonance frequencies in the range expected from simulations. The work also provides an overview of the basic properties of superconductors and of lumped element resonator theory. A lumped elements model was introduced to describe qualitatively the scattering parameters of a spiral resonator capacitively coupled to a feedline and to understand the behavior of its quality factor.

## Acknowledgement

I want to thank Prof. Dr. Alexey Ustinov for giving me the opportunity to work in his group and Dr. Martin Weides for his most patient and throughout helpful, constructive supervision. I am also grateful to Tobias Bier for fabricating the measured resonators and I thank Philipp Jung for helping me with IT problems at the beginning of my work, as I do thank all members of the Ustinov group for the help I received.

# Bibliography


[1] G. V. Eleftheriades and K. G. Balmain. *Negative-refraction metamaterials: fundamental principles and applications.* John Wiley & Sons, 2005.

[2] V. G. Veselago. The electrodynamics of substances with simultaneously negative values of $\epsilon$ and $\mu$. *Physics-Uspekhi*, 10(4):509–514, 1968.

[3] C. Kurter, A. P. Zhuravel, J. Abrahams, C. L. Bennett, A. V. Ustinov, and S. M. Anlage. Superconducting rf metamaterials made with magnetically active planar spirals. *Applied Superconductivity, IEEE Transactions on*, 21(3):709–712, 2011.

[4] B. Ghamsari, J. Abrahams, S. Remillard, and S. Anlage. High-temperature superconducting spiral resonators for metamaterials applications. *Applied Superconductivity, IEEE Transactions on*, 23(3), 2012.

[5] H. Kamerlingh Onnes. The superconductivity of mercury. *Comm. Phys. Lab. Univ. Leiden*, 122:124, 1911.

[6] C. Kittel. *Einführung in die Festkörperphysik.* Oldenbourg, 15th edition, 2013.

[7] G. Muenster. *Quantentheorie.* De Gruyter, 2nd edition, 2010.

[8] M. Neuwirth. *Investigation of field distribution in superconducting microwave resonators.* Bachelor thesis, Karlsruhe Institute of Technology, 2013.

[9] S. Hunklinger. *Festkörperphysik.* Oldenbourg, 3rd edition, 2011.

[10] M. Tinkham. *Introduction to Superconductivity.* Dover Publications, second edition, 2004.

[11] B. S. Deaver and W. M. Fairbank. Experimental evidence for quantized flux in superconducting cyclinders. *Physical Review Letters*, 7(2):43–46, 1961.

[12] E. Babaev, J. Carlström, J. Garaud, M. Silaev, and J. M. Speight. Type-1.5 superconductivity in multiband systems: Magnetic response, broken symmetries and microscopic theory–a brief overview. *Physica C: Superconductivity*, 479:2–14, 2012.

[13] W. Buckel and R. Kleiner. *Superconductivity.* Wiley-VCH, second edition, 2004.

[14] W. Greiner. *Klassische Elektrodynamik.* Harri Deutsch Verlag, 6th edition, 2002.

[15] D. M. Pozar. *Microwave Engineering.* Wiley, 3rd edition edition, 2005.

[16] M. Goppl, A. Fragner, M. Baur, R. Bianchetti, S. Filipp, J. M. Fink, P. J. Leek, G. Puebla, L. Steffen, and A. Wallraff. Coplanar waveguide resonators for circuit quantum electrodynamics. *Journal of Applied Physics*, 104(11):113904–113904, 2008.

[17] D. Wisbey, A. Reinisch, W. Gardner, J. Brewster, and J. Gao. New method for determining the quality factor and resonance frequency of superconducting micro-resonators from sonnet simulation. *Bulletin of the American Physical Society*, 58(1), 2013.

[18] http://www.tannereda.com/products/l-edit pro.

[19] D. Bothner, T. Gaber, M. Kemmler, D. Koelle, and R. Kleiner. Improving the performance of superconducting microwave resonators in magnetic fields. *Applied Physics Letters*, 98(10):102504–102504, 2011.

[20] http://www.sonnetsoftware.com/about/.

[21] J. Gao. *The Physics of Superconducting Microwave Resonators*. PhD thesis, California Institute of Technology, 2008.

[22] Ch. Enss and S. Hunklinger. *Tieftemperaturphysik*. Springer, 2000.